A neutrinophilic dark matter model with a scalar portal

Ein neutrinophiles Modell für dunkle Materie mit einem skalaren Portal

Bachelorarbeit

Eingereicht von:
Lambert Thüner

Westfälische Wilhelms-Universität Münster
Institut für Theoretische Physik
AG Klasen

Erstgutachter: Prof. Dr. Michael Klasen
Zweitgutachter: PD Dr. Karol Kovařík

Münster, September 2023

Declaration of Academic Integrity

I hereby confirm that this thesis, entitled A NEUTRINOPHILIC DARK MATTER MODEL WITH A SCALAR PORTAL is solely my own work and that I have used no sources or aids other than the ones stated. All passages in my thesis for which other sources, including electronic media, have been used, be it direct quotes or content references, have been acknowledged as such and the sources cited. I am aware that plagiarism is considered an act of deception which can result in sanction in accordance with the examination regulations.

Münster, September 2023

Lambert Thüner

I consent to having my thesis cross-checked with other texts to identify possible similarities and to having it stored in a database for this purpose.

I confirm that I have not submitted the following thesis in part or whole as an examination paper before.

Münster, September 2023

Lambert Thüner

Contents

1 Introduction **1**

2 The Particle Content of the Universe **3**

2.1 (Neutrinos in) the Standard Model of particle physics 3

2.2 Weakly Interacting Massive Particles 4

2.3 The model for dark matter of this thesis 4

3 Expansion, Thermodynamics and History of the Universe **7**

3.1 The Friedmann equations 7

3.2 Thermodynamics of the expanding universe 9

3.3 The Big Bang and the early universe 11

4 Dark Matter Freeze-Out **13**

4.1 The Boltzmann equation for the number density 13

4.2 The Boltzmann equation for the yield 15

4.3 Simplifying the thermal averages 16

5 Annihilation Cross Sections and Decay Widths of the Dark Matter Model **21**

5.1 Mandelstam variables 22

5.2 Decay width of the scalar portal 23

5.2.1 Decay width for the decay $\phi \to \nu\bar{\nu}$ 23

5.2.2 Decay width for the decay $\phi \to D\bar{D}$ 26

5.3 Cross section of $D\bar{D} \to \nu\bar{\nu}$ 26

5.4 Cross section of $D\bar{D} \to \phi\phi$ 29

5.4.1 t-channel and u-channel 31

5.4.2 Interference term 33

5.4.3 Total cross section 34

5.5 $\langle \sigma v \rangle$ at rest 35

6 Numerical Solution of the Boltzmann Equation **37**

6.1 Implementation in `MATLAB` 37

6.2 Evolution of the yield with temperature 38

6.3 Interaction rates and $\langle \sigma v_{\mathrm{Møl}} \rangle$ 41

6.4 Restriction through the final relic density 42
6.5 Comparison to the results from micrOMEGAs 43
6.6 Using bisection to restrict the parameter space 46

7 Restrictions from the Measured Neutrino Flux **49**
7.1 Limits on the parameter space 50

8 Conclusion and Outlook **53**

A Feynman Rules **55**

B Identities Involving Dirac Matrices **57**

C Simulation Code in MATLAB **59**

Bibliography **65**

1 Introduction

One of the most confounding problems in modern physics is the plethora of evidence pointing to the fact that most of the mass in the universe is not made up of the known particles. In fact, only roughly 5% of the total mass is made of ordinary matter. The other 95% is what is known as the dark sector. This contains a dark matter (DM) component making up 27% of the universe's mass and the rest is what is known as dark energy [1]. While the true nature of both dark energy and DM is not yet known, this thesis deals with one model for DM and as such, the topic of dark energy is not dealt with beyond this point.

The term DM refers to the fact that it is invisible in the sense that it does not interact electromagnetically. However, its presence can be observed because it interacts gravitationally. The first evidence for such matter was discovered in the 1930s by Zwicky and Smith who investigated the velocity dispersions of galaxy clusters. These were much higher than could be explained with the visible mass present but it took until the 1970s until this discrepancy was attributed to the presence of additional mass. Furthermore, the observations of the rotation curves of galaxies also pointed to the presence of additional mass. Since most of the mass lies at the center of the galaxy the radial velocity should decrease with $1/\sqrt{r}$. What was observed instead is a roughly constant radial velocity for large radii r [3]. This is illustrated in Fig. 1.1.

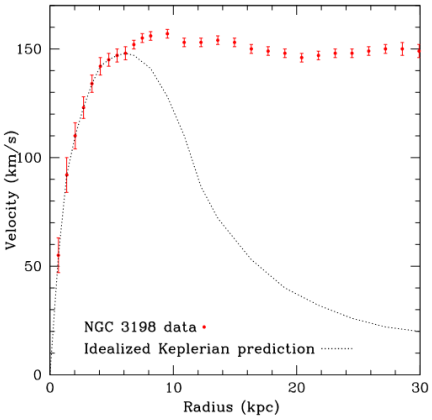

Figure 1.1: Measured rotation velocities in the galaxy NGC3198 compared to the idealized Keplerian behaviour, where $v \propto 1/\sqrt{r}$ for large radii r [2].

Since then, more and more evidence for the existence of DM has been found. This includes the spectrum of the cosmic microwave background (CMB) from which the above mass fractions are derived as well as the modeling of structure formation in the early universe and observed effects of gravitational lensing [2, 3].

While the evidence for DM is abundant, as of today, the nature of this matter is largely unknown. DM could be a single new elementary particle but more complex models as well as compound particles also remain viable explanations [3]. The investigations of the validity of such models is one of the interesting connections between particle physics and cosmology

which this thesis tries to study.

There are three approaches currently under experimental and theoretical investigations in an effort to detect DM or at least limit the possible candidates. Direct detection experiments try to observe the interaction of a DM particle with known matter. Such interactions should be exceedingly rare if they exist at all and are therefore very difficult to detect. Ongoing experimental efforts in this regard include time-projection chambers filled with liquid Xenon such as the XENONnT experiment which aims to detect the scattering of DM particles off of Xenon nucleii [4]. Searches at colliders try to produce DM through the collision of known particles [5].

Finally, there is also a plethora of indirect detection methods which are in a sense the inverse of the collider searches. DM models that allow for the annihilation into SM particles will produce fluxes of SM particles which are in principle measurable. Hence, the observation of cosmic γ-rays as well as neutrinos can put limits on the cross section for these processes which are be already constrained by the fact that the model also needs to explain the amount of DM measured today [5].

The specific model in this thesis is neutrinophilic, i.e. the hidden sector of DM particles only couples to neutrinos. Therefore, the only viable detection mechanism is indirect detection through cosmic neutrinos. At present, these fluxes do not provide an additional constraint on the parameter space of the model as the observed DM density today - usually referred to as the relic density - is always the stronger limitation.

2 The Particle Content of the Universe

The most accurate theory to describe elementary particles and their interactions presently available is known as the Standard Model (SM). It is able to accurately explain the interactions of all particles detected to date as well as three out of four of the known elementary forces: the electromagnetic, weak and the strong interaction [6].
The theory has the form of a quantum field theory in which the individual particles are represented as excited states of fundamental fields. Its core element is a Lagrangian which gives the equations of motion for the fields from the minimization of the action as the Euler-Lagrange equations [7].
The SM is compatible with special relativity. This means that its equations of motion are invariant when the frame of reference is changed. This corresponds to an invariance of the Lagrangian[1] under Lorentz transformations and restricts the kind of terms which can appear in the Lagrangian as well as the possible behaviors of the fields under Lorentz transformations [7]. This is explained in more detail when the DM model investigated in this thesis is introduced at the end of this chapter.
It is not useful for the purposes of this thesis to discuss all particles of the SM in detail as the extension of the SM investigated in this thesis as a model for DM only couples to neutrinos. Instead, only a brief introduction on neutrinos is given in the following Section 2.1.
Regardless of its success, the SM in its current form is incomplete. For one, there is the dark sector mentioned in the previous chapter. Section 2.2 elaborates on WIMPs as one class of candidates for DM and Section 2.3 introduces the specific type of WIMP investigated in this thesis.

2.1 (Neutrinos in) the Standard Model of particle physics

Neutrinos were originally postulated in 1930 to explain the continuous energy spectrum of β-decays as massless Spin-$^1/_2$ particles. They only interact with other particles through the weak force and are therefore notoriously hard to detect [8].
Today, there are three known neutrino flavors corresponding to the three charged leptons - the electron, muon, and tau. In contrast to the charged leptons, neutrinos do not possess an

[1] The equations of motion come from the action, not the Lagrangian itself. So in principle, the Lagrangian could vary under Lorentz transformations as long as the action is invariant. But if the Lagrangian is invariant, then so is the action.

electric charge and therefore only interact with other particles through the weak interaction. They are also considered to be massless in the standard model [8].
However, the observation of neutrino oscillations shows that neutrinos must possess a mass, albeit a very small one. The exact masses are currently under experimental investigation but are below 1 eV [9].
It is also not yet clear whether neutrinos are Dirac fermions, meaning neutrinos and anti-neutrinos are different particles, or Majorana fermions, meaning that neutrinos are their own anti-particles. In the latter case, there is the possibility for a neutrino-less double-β decay which is currently being looked for by multiple experiments [10]. The calculations made in this thesis assume neutrinos to be Dirac fermions.

2.2 Weakly Interacting Massive Particles

As mentioned in the introduction there are numerous viable models for DM on mass scales of the DM candidate from a few eV all the way up to macroscopic masses. One of the leading paradigms is known as Weakly Interacting Massive Particles (WIMPs) [4].
The term originates from the fact that particles with masses in the GeV to TeV range naturally have annihilation cross sections similar to those of the weak force (in the order of $10^{-26}\,\mathrm{cm}^3/\mathrm{s}$) in order to produce the observed relic density via freeze-out. As such both models where the new particles interact via the weak force and where the new particles interact via a new force of similar strength have been studied extensively and the term WIMP has been taken to mean both kinds of models [3].

2.3 The model for dark matter of this thesis

The model consists of the Standard Model (SM) sector as the visible sector with a hidden sector made up of Dirac fermions D (and $\bar{D}$) with mass m_D and a scalar portal ϕ with mass m_ϕ. The D fermion is the DM candidate and both fields do not possess charges under the SM gauge group, hence the term 'hidden'. However, the two sectors are connected via the scalar portal ϕ which only has couplings with the neutrinos of the visible sector and the DM candidate. The Lagrangian after electroweak symmetry breaking is written as

$$\mathcal{L} = \mathcal{L}_\mathrm{SM} + \mathcal{L}_\mathrm{kin} + \mathcal{L}_\mathrm{int}\,, \tag{2.1}$$

where $\mathcal{L}_{\mathrm{SM}}$ is the SM Lagrangian and the Lagrangian of the hidden sector is

$$\begin{aligned}\mathcal{L}_{\mathrm{kin}} &= \frac{1}{2}\partial_\mu\phi\partial^\mu\phi - \frac{1}{2}m_\phi^2\phi^2 + \bar{D}(\hat{\imath}\gamma^\mu\partial_\mu - m_{\mathrm{D}})D,\\ \mathcal{L}_{\mathrm{int}} &= -\phi\bar{\nu}_{\mathrm{i}}(g_{\mathrm{n_{ij}}} + \hat{\imath}g'_{\mathrm{nij}}\gamma^5)\nu_{\mathrm{j}} - \phi\bar{D}(g_{\mathrm{x}} + \hat{\imath}g'_{\mathrm{x}}\gamma^5)D\,. \end{aligned} \tag{2.2}$$

The notation of this Lagrangian makes use of two conventions which make the notation more compact: one is Einstein's summation convention where indices appearing multiple times in a product are summed over. Lowercase Latin letters $i, j, ...$ correspond to sums from 1 to 3 while lowercase Greek letters $\mu, \nu, ...$ run from 0 to 3.
Secondly, this thesis uses natural units where the numerical values of the reduced Planck constant $\hbar$, the speed of light c and the Boltzmann constant k_{B} are set to 1.
For simplicity, the couplings $g_{\mathrm{n_{ij}}}$ and g'_{nij} are taken to be diagonal and the same for the three neutrino species, i.e., $g_{\mathrm{n_{ij}}} = g_{\mathrm{n}}\delta_{\mathrm{ij}}$ and $g'_{\mathrm{n}ij} = g'_{\mathrm{n}}\delta_{\mathrm{ij}}$. This means that only neutrinos of the same flavor can interact via the scalar ϕ and the strength of the interaction is the same for all three flavors.
The Lagrangian $\mathcal{L}$ encodes all information about the equations of motions of the particles and their interactions. The term $\mathcal{L}_{\mathrm{kin}}$ is the equivalent to the kinetic energy in the Lagrangians of classical mechanics. The equations of motion can be obtained by partially differentiating after the fields. Ignoring the interaction term $\mathcal{L}_{\mathrm{int}}$, these are the Klein-Gordon equation for the scalar field ϕ and the Dirac equation for the (anti-)fermion field D ($\bar{D} = D^\dagger\gamma^0$) as these equations are the equations of motion for a free scalar and a free spin-1/2 particle [6].
$\mathcal{L}_{\mathrm{int}}$ specifies the kind of interactions that are possible as well as the strength of the coupling for these interactions. The presence of the scalar ϕ and the fermion as well as anti-fermion fields in all of its summands implies that all interactions are mediated via the scalar ϕ which allows annihilation of fermion anti-fermion pairs as well as scattering processes and decays of ϕ into both $D\bar{D}$-pairs and neutrinos and anti-neutrinos. However, decays of D and $\bar{D}$ are impossible since the fields only appear in combination in the interaction terms and never alone. The factors in the summands of $\mathcal{L}_{\mathrm{int}}$ other than the fields are known as the vertex factors. They are matrix valued with γ^5 being the 'fifth' Dirac matrix. This also appears in the vertex factors of the weak interaction where a factor $(1 - \gamma^5)/2$ ensures that only left-chiral particles interact via the weak force.[7]
This thesis will not use $\mathcal{L}$ explicitly after this point. As it encodes all information about the model it is however playing a crucial role in the background, specifically when calculating decay widths and cross sections for the processes possible in this model in Chapter 5. This will be done using Feynman rules which are summarized in Appendix A.
The decay widths and cross sections determine the relic density. This connection is explained in Chapter 4. Since the relic density can be measured, this restricts the viable parameter

space of the model, that is the values of the couplings and masses. Chapter 6 calculates the relic density for different parameters. In addition, the decays of the scalar portal ϕ and annihilation processes produce neutrinos. Their flux is observable and also restricts the viable parameters which is investigated in Chapter 7.

3 Expansion, Thermodynamics and History of the Universe

To understand the universe as it is observed today, it is crucial to reconstruct the events in the past that lead it to its current state. Presently, the best theory to depict the development of the universe is known as the Lambda cold DM model (ΛCDM). Other than the particles of the SM, it also takes into account dark energy and DM [11].
Hence, the intricacies of this model require both the relativistic dynamics and the particle interactions given by the SM in addition to the dark sector. Section 3.1 goes over the basic relativistic dynamics which imply the existence of a Big Bang. After that, Section 3.2 introduces some thermodynamics that are helpful to understand the key results of ΛCDM which are given in Section 3.3 with a focus on the role of the neutrinos and cold DM. The thermodynamics are used in the following chapters that deal with the Boltzmann equation for DM freeze-out while the results of ΛCDM impose some constraints on the model.

3.1 The Friedmann equations

This section is based on the first section in [11] and a shorter, freely accessible overview can be found in the first section of [12].
In general, the dynamics of the universe due to gravity are described by the tensor-valued Einstein equation. However, the universe is both isotropic and homogenous on large scales. The CMB shows that this is also true in the early universe. With this as an assumption, the Einstein equation reduces to two ordinary differential equations.
The first of these equations, referred to as the first Friedmann equation, is

$$\left(\frac{\dot{a}}{a}\right)^2 = \frac{8\pi G}{3}\rho - \frac{k}{a^2}\,. \tag{3.1}$$

G is Newton's gravitational constant and ρ the total energy density. k is a parameter describing the curvature of the universe.
$a(t)$ is called the scale factor and describes the expansion of the universe. A doubling of the scale factor causes the physical distance $r_{\text{phys.}}$ between two comoving points in space to double as well, so $r_{\text{phys.}}(t) = a(t) r_{\text{com.}}$. This is illustrated in Fig. 3.1. The normalization of

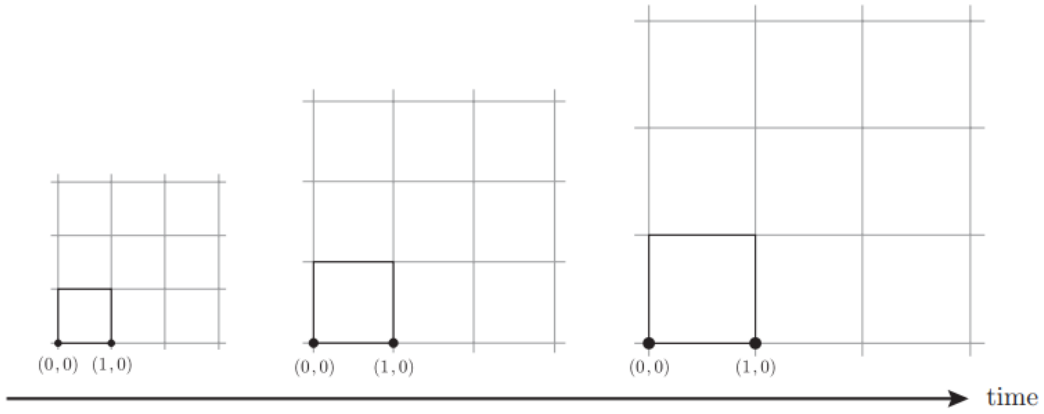

Figure 3.1: An illustration of the effect of the scale factor $a(t)$: The physical distance between two points of a comoving coordinate system is proportional to it. In addition, $a(t)$ increases with time. Figure take from [11, p. 7].

the scale factor can be chosen freely and so it is useful to define $a = 1$ at present day.
The relative change of a with time is the Hubble parameter $H = \dot{a}/a$, which is time-dependent. Plugging this into Eq. 3.1 leads to

$$H^2 = \frac{8\pi G}{3}\rho - \frac{k}{a^2}\,. \tag{3.2}$$

To solve this equation, the relation between the energy density ρ and the scale factor is needed. The relevant contributions are **r**adiation, **m**atter, **c**old DM and dark energy (Λ). The total energy density is the sum of these three contributions. This allows Eq. 3.2 to be written as

$$H^2 = \frac{8\pi G}{3}(\rho_\mathrm{r} a^{-4} + \rho_\mathrm{m} a^{-3} + \rho_\mathrm{c} a^{-3} + \rho_\Lambda) - k a^{-2} \tag{3.3}$$

where the densities ρ_i are the densities today.
Defining the dimensionless density parameters

$$\Omega_\mathrm{i} = \frac{\rho_\mathrm{i}}{\rho_\mathrm{crit}}\ , \mathrm{i} = \mathrm{r, m, c}, \Lambda, \mathrm{k} \text{ with } \rho_\mathrm{crit} = \frac{3H_0^2}{8\pi G} \text{ and } \rho_\mathrm{k} = \frac{-3k}{8\pi G} \tag{3.4}$$

where H_0 is today's Hubble parameter, gives the form

$$\left(\frac{H}{H_0}\right)^2 = \Omega_\mathrm{r} a^{-4} + \Omega_\mathrm{c} a^{-3} + \Omega_\mathrm{c} a^{-3} + \Omega_\Lambda + \Omega_\mathrm{k} a^{-2} \tag{3.5}$$

to the first Friedmann equation. This form allows for easy comparison between the four contributions. For $a \ll 1$ the universe was dominated by radiation while the relative importance

of matter and especially dark energy increases with the scale factor.
This form also makes it possible to link the energy densities to the curvature k:

$$\Omega \equiv \Omega_\mathrm{r} + \Omega_\mathrm{m} + \Omega_\mathrm{c} + \Omega_\Lambda = 1\,, \tag{3.6}$$

implies $k = 0$.
Today, we have $\Omega_\mathrm{k} \leq 0.01$ [1] and because its impact scales with a^{-2}, this means that the influence of the curvature in the first Friedmann equation is always negligible.
This form is also the reason to write the observed energy densities in terms of the critical density ρ_crit as Ω_i or in the form $\Omega_\mathrm{i}h^2$ where h is value of the Hubble parameter in units of 100 $\mathrm{Mpc\,km^{-1}s^{-1}}$. The latter is independent of the exact value of H and thus often preferable.
One of the most important implications of the first Friedmann equation is that because H is positive today and the curvature term is negligible, a has monotonically increased with time (and will do so in the future as well) and at some point been equal to 0. At this point in time, the universe was a singularity of infinite density and no spacial extension.
There is no current theory for describing such a state or anything before the singularity. However, at some point this singularity started to expand. This is known as the Big Bang and the modeling of its aftermath produces the best theory for the history of the universe currently available.

3.2 Thermodynamics of the expanding universe

There is strong evidence that the early universe was in local thermal equilibrium. This evidence comes from the near perfect black-body spectrum of the Cosmic Microwave Background (CMB). Its origin will be discussed in the following section. This means that the results of equilibrium thermodynamics can be used to describe the evolution of thermodynamical quantities such as the energy density ρ and the number density n.
One of the standard results of quantum statistical mechanics is that the phase space density has the form

$$\frac{g}{(2\pi)^3} \times f(p) = \frac{g}{(2\pi)^3} \times \frac{1}{\exp\left(E(p) - \mu\right)/T \pm 1} \tag{3.7}$$

where the $+$ of the Fermi-Dirac distribution is for fermions and the $-$ of the Bose-Einstein distribution for bosons. g accounts for internal degrees of freedom. It is 2 for Dirac particles and photons, 1 for scalar bosons and 3 for massive vector bosons.

In the non-relativistic case of low temperatures $E(p) - \mu > T$ both distributions are well approximated by the Maxwell-Boltzmann distribution

$$f(p) = \exp\left(\frac{\mu - E(p)}{T}\right) . \tag{3.8}$$

The temperature dependent chemical potential μ can be neglected in the early universe.
From the phase space densities, the density $W(t)/V$, where V is the physical volume and therefore scales with a^3, of a thermodynamical quantity $w(E)$[2] is obtained by calculating the integral

$$\frac{W(t)}{V} = \frac{g}{(2\pi)^3} \int \mathrm{d}^3 p f(E,t) w(E) . \tag{3.9}$$

However, this formula only works for one particle species. The key to generalize it for arbitrary particle species is the concept of effective degrees of freedom. This is best explained for the concrete example of the energy density ρ. Here, there are three relevant cases with analytical solutions for a particle species with mass m:

$$\begin{aligned} \rho &= \frac{g}{(2\pi)^3} \int \mathrm{d}^3 p f(E) E \\ &= \begin{cases} gm \left(\frac{mT}{2\pi}\right)^{3/2} \exp\left(-m/T\right) & \text{n.r. approximation for } T \ll m \\ \frac{\pi^2}{30} g T^4 & \text{relativistic bosons } T \gg m \\ \frac{7}{8}\frac{\pi^2}{30} g T^4 & \text{relativistic fermions } T \gg m \end{cases} \end{aligned} \tag{3.10}$$

So ρ for relativistic particles scales with T^4 while ρ for non-relativistic particles is exponentially suppressed.
The energy density of the radiation ρ_r is the sum of contributions of all relativistic particles species. These do not have to be in thermal equilibrium and thus have different temperatures. Therefore, this leads to

$$\rho = \frac{\pi^2}{30} g_\mathrm{eff}(T) T^4 \quad \text{with} \quad g_\mathrm{eff}(T) = \sum_\mathrm{Bosons} g_B \frac{T_B^4}{T^4} + \frac{7}{8} \sum_\mathrm{Fermions} g_F \frac{T_F^4}{T^4} \tag{3.11}$$

where T now refers to the photon temperature. The quantity $g_\mathrm{eff}(T)$ is the effective number of degrees of freedom and can be found in tabulated form for the particle content of the SM. This thesis uses the degrees of freedom calculated in [13].
Crucially, Eq. 3.11 gives a connection between Hubble parameter H and temperature T

$$H = \sqrt{\frac{8\pi G}{3}\rho} = \sqrt{\frac{4\pi^3 G}{45} g_\mathrm{eff}} T^2 \tag{3.12}$$

[2] There will be no dependence on location because of homogeneity or momentum because of isotropy.

and therefore also time t and temperature T. The next chapter will make use of this connection to obtain a differential equation in terms of temperature T for the number density.
In the same way g_{eff} is defined for the energy density ρ, the effective degrees of freedom h_{eff} for the entropy density $\tilde{s} = S/V$ are defined to fulfill

$$\tilde{s} = \frac{2\pi^2}{45} h_{\text{eff}}(T) T^3 \quad \text{with} \quad h_{\text{eff}}(T) = \sum_{\text{Bosons}} g_B \frac{T_B^3}{T^3} + \frac{7}{8} \sum_{\text{Fermions}} g_F \frac{T_F^3}{T^3} \,. \tag{3.13}$$

Because entropy S is conserved in equilibrium, the entropy density $\tilde{s}$ is proportional to a^{-3}.

3.3 The Big Bang and the early universe

Starting from the Big Bang, the first $\sim 10^{-43}\,\text{s}$ cannot be described by current theories as the conditions here require a workable quantum field theory of gravity which currently does not exist. The following first second of the universe is filled with fascinating events which would take up too much space to discuss here. Baumann's lecture notes [11] give a good overview and so does the classic textbook by Kolb and Turner [14]. The contents of this section can be found in both sources.
To describe it shortly: Because of the continuing expansion of the universe the temperature drops rapidly at first from an initial value of 10^{18}GeV at around $\sim 10^{-43}\,\text{s}$ down to about $1\,\text{MeV}$, $1\,\text{s}$ after the Big Bang. During this time, particles receive their masses through the Higgs mechanism and quarks and gluons form mesons and baryons. Before that, there also must have been a period of accelerated expansion known as inflation as otherwise the universe today should not be as homogenous and isotropic as it is observed to be on cosmic scales.
After the temperature T drops below $1\,\text{MeV}$, the interaction rate Γ of the processes

$$\begin{aligned} n + \nu_{\text{e}} &\leftrightarrow p + e^- \\ p + \bar{\nu}_{\text{e}} &\leftrightarrow n + e^+ \end{aligned} \tag{3.14}$$

becomes negligible against the expansion rate H. Before this point, these processes kept the abundances of neutrons, protons and neutrinos at their equilibrium distribution and thus the amount of protons and neutrons is determined by the amount present at this point. This is known as a freeze-out and the same mechanism can create an abundance of DM particles. It is discussed in more detail in the next chapter.
As the model for DM investigated in this thesis produces neutrinos through the decay of the scalar ϕ and annihilation processes of $D\bar{D}$, both of these processes need to be negligible for temperatures $T < 1\,\text{MeV} \Longleftrightarrow t > 1\,\text{s}$. Otherwise, there would be an additional amount of neutrinos which would impact the decoupling point of protons and neutrons from thermal

equilibrium and thus the ratio of protons to neutrons.
However, since the measured ratio of protons to neutrons today requires the decoupling to be at $T = 1\,\mathrm{MeV}$ this cannot be. This imposes restrictions on the parameter space of the DM model: The life expectancy of the scalar ϕ should be no greater than one second

$$\Gamma^{-1}_{\phi\to\nu\overline{\nu}} < 1\,\mathrm{s} \tag{3.15}$$

and the decoupling of the fermion D from thermal equilibrium needs to occur at a temperature T_f with

$$T_\mathrm{f} > 1\,\mathrm{MeV}\,. \tag{3.16}$$

The analysis of the model will show that the restriction on the life expectancy is only relevant for $m_\phi \lll m_\mathrm{D}$ and the restriction on the freeze-out temperature is dealt with if $m_\mathrm{D} \gtrsim 1\,\mathrm{GeV}$. Thus, this model is part of the WIMP-family of DM models.
After 3 min or at around 100 keV the Big Bang nucleosynthesis begins and creates nucleii up to Lithium-7, although almost exclusively Helium and Hydrogen. It ends less than 15 min after the Big Bang when the conditions are no longer sufficient for further fusion reactions.
The final relevant step for this thesis occurs around 380 000 yrs after the Big Bang. At this point, the photons decouple from thermal equilibrium, allowing the formation of atoms and creating what today has become the CMB. This almost perfect black body spectrum allows a multitude of insights into the universe. One of them is the most precise measurement of the amount of cold DM to date, giving [1]

$$\Omega_\mathrm{c} h^2 = 0.120 \pm 0.001\,. \tag{3.17}$$

4 Dark Matter Freeze-Out

While there are multiple possible mechanisms to create the observed abundance of DM this thesis will focus on freeze-out. This occurs when the interaction rate Γ of processes keeping particles in thermal equilibrium drops below the rate of expansion, the Hubble parameter H. Fig. 4.1 illustrates the expected resulting behavior of the number density. The interaction rate is given as $\Gamma = n\langle\sigma v\rangle$ where n is the number density of the particle and $\langle\sigma v\rangle$ is the thermal average of the cross section for the processes times a velocity v.

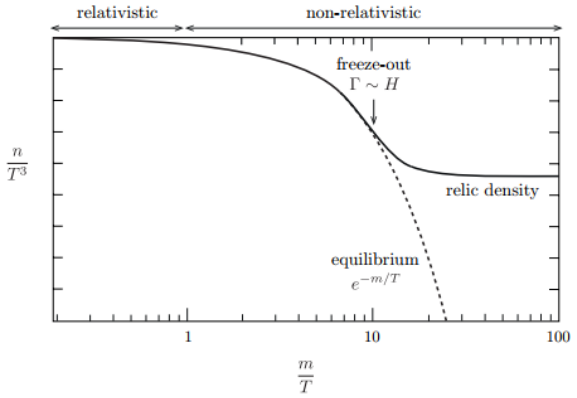

Figure 4.1: Schematic illustration of particle freeze-out. At high temperatures $T \gg m$, where the particles move at relativistic velocities, the number density n stays in thermal equilibrium. At low temperatures with $T \ll m$ the interaction rate $\Gamma = n\langle\sigma v\rangle$ drops below the expansion rate H and so the number density freezes out to remain at a much higher value than the equilibrium distribution. Figure taken from [11].

Section 4.1 introduces the relevant differential equation for the number density n which describes freeze-out for a DM model with only one stable particle. The following Section 4.2 turns this into a differential equation for the yield Y which is easier to use as Y is independent of the scale factor a and Section 4.3 simplifies elements of the differential equation.
The original derivations of this chapter for the purpose of describing DM freeze-out have been done by Gondolo and Gelmini in [15].

4.1 The Boltzmann equation for the number density

In general, tracking the evolution of a particle species requires the Boltzmann equation

$$L[f] = C[f]\,, \tag{4.1}$$

which describes the evolution of the phase space density $f(p, x, t)$ over time. f should be homogenous and isotropic in space as the same holds for the observed universe and thus only depends on the energy E and time t. So it is connected to the number density n via

$$n = \int \mathrm{d}n = \int \mathrm{d}^3 p f(E,t) \frac{g}{(2\pi^3)}\,, \tag{4.2}$$

where the factor g accounts for possible internal degrees of freedom because of spin.
L (the Liouville operator) contains the terms tracking the net change of f in time, while the collision term C describes the effects of annihilations into different particles as well as scattering.
In the case of two DM particles species and under the additional assumption that all other particles which the DM particles interact with are in thermal equilibrium[3] Eq. 4.1 leads to coupled differential equations for the number densities of the DM particles n_1 and n_2 - in the model investigated in this thesis presented in Section 2.3 the two DM particles are D and its anti-particle $\bar{D}$:

$$\begin{aligned} \dot{n_1} + 3Hn_1 &= -\langle \sigma v_{\mathrm{Møl}} \rangle (n_1 n_2 - n_1^{\mathrm{eq}} n_2^{\mathrm{eq}}) \\ \dot{n_2} + 3Hn_2 &= -\langle \sigma v_{\mathrm{Møl}} \rangle (n_1 n_2 - n_1^{\mathrm{eq}} n_2^{\mathrm{eq}})\,. \end{aligned} \tag{4.3}$$

n_1^{eq} and n_2^{eq} are the number densities in thermal equilibrium, that is Eq. 4.2 with the Fermi-Dirac or Bose-Einstein distribution for fermions or bosons respectively. So the collision term on the right hand side of the differential equations results in a depletion of the number densities towards their equilibrium distributions. The term $3Ha^3$ on the left hand side represents the change of number density through the expansion of the universe, that is, the change of the scale factor $H = \dot{a}/a$. The left hand sides can also be written as

$$\dot{n} + 3Hn = \frac{1}{a^3} \frac{\mathrm{d}(na^3)}{\mathrm{d}t}\,, \tag{4.4}$$

meaning that the number of particles in a covariant volume only changes because of annihilations, as is to be expected.
So these differential equations match the qualitative assessment from the previous chapter: There are two competing effects on the number density. The expansion leads to a decrease of n while the interaction with other particles results in a change towards thermal equilibrium.

[3] This is another reason this thesis only investigates $m_{\mathrm{D}} \geq 1\,\mathrm{GeV}$: For lower m_{D} this assumption might not hold for neutrinos, which decouple around 1 MeV (see Section 3.3), before the relic density is set.

The thermally averaged cross section times velocity $\langle \sigma v_{\text{Møl}} \rangle$ in the right hand side is given as

$$\langle \sigma v_{\text{Møl}} \rangle = \frac{\int \mathrm{d}n_1^{\text{eq}} \, \mathrm{d}n_2^{\text{eq}} \, \sigma v_{\text{Møl}}}{n_1^{\text{eq}} n_2^{\text{eq}}} \,, \tag{4.5}$$

where $v_{\text{Møl}}$ is the Møller velocity

$$v_{\text{Møl}} = \sqrt{|\vec{v_1} - \vec{v_2}|^2 - |\vec{v_1} \times \vec{v_2}|^2} \,. \tag{4.6}$$

The cross section σ is the sum of the cross sections for all annihilation channels. For the concrete model of Section 2.3 these are the processes $D\bar{D} \to \phi\phi$ and $D\bar{D} \to \nu\bar{\nu}$.
There is no reason to assume an asymmetry in the initial production of D and $\bar{D}$ and so there is $n_1 = n_2 = n$. Thus, the coupled differential equations Eq. 4.3 become identical because the indices 1 and 2 are irrelevant and the differential equation for the number density reads

$$\dot{n} + 3Hn = -\langle \sigma v_{\text{Møl}} \rangle (n^2 - n_{\text{eq}}^2) \tag{4.7}$$

Working with this decoupled differential equation Eq. 4.7 is not ideal for two reasons: Firstly, one would need to track the scale factor a and the Hubble parameter H in addition to the number density n. Using a differential equation for the yield $Y = n/\tilde{s}$ instead, with $\tilde{s}$ being the entropy density, circumvents these problems. The next section derives this differential equation for Y.
Secondly, the equation for $\langle \sigma v_{\text{Møl}} \rangle$ and the equilibrium densities n_{eq} can be brought into forms that are easier to work with. This is the topic of the last Section 4.3 of this chapter.

4.2 The Boltzmann equation for the yield

From the Boltzmann equation Eq. 4.7 one obtains

$$\begin{aligned} \dot{Y} &= \frac{1}{\tilde{s}a^3} \frac{\mathrm{d}(na^3)}{\mathrm{d}t} + na^3 \frac{\mathrm{d}\left(\tilde{s}a^3\right)^{-1}}{\mathrm{d}t} = \frac{1}{\tilde{s}a^3} \frac{\mathrm{d}(na^3)}{\mathrm{d}t} \\ &= -\frac{1}{\tilde{s}} \langle \sigma v_{\text{Møl}} \rangle (n^2 - n_{\text{eq}}^2) \\ &= -\tilde{s} \langle \sigma v_{\text{Møl}} \rangle (Y^2 - Y_{\text{eq}}^2) \end{aligned} \tag{4.8}$$

as the differential equation for the yield Y. Since $\tilde{s} \propto a^{-3}$, the time derivative of $\tilde{s}a^3$ vanishes. Having time as the independent variable is inconvenient as the freeze-out happens at different times depending on the chosen parameters of the model, especially on m_{D}, and so the interval within which decoupling happens would need to be estimated first for each mass.

Furthermore, the equilibrium distributions as well as $\langle \sigma v_{\text{Møl}} \rangle$ naturally depend on the temperature T. Hence, the most convenient choice for the independent variable is $x = m/T$ as the freeze-out occurs at around $x = 20$ and Y is almost constant for $x \gtrsim 200$ [11, 12].
The chain rule gives

$$\dot{Y} = \frac{\mathrm{d}Y}{\mathrm{d}x} \frac{\mathrm{d}x}{\mathrm{d}a} \dot{a} \tag{4.9}$$

and so the differential equations becomes

$$\frac{\mathrm{d}Y}{\mathrm{d}x} = -\frac{s}{Ha} \frac{\mathrm{d}a}{\mathrm{d}x} \langle \sigma v_{\text{Møl}} \rangle (Y^2 - Y_{\text{eq}}^2) \,. \tag{4.10}$$

This can be simplified further to

$$\frac{\mathrm{d}Y}{\mathrm{d}x} = \frac{1}{3H} \frac{\mathrm{d}s}{\mathrm{d}x} \langle \sigma v_{\text{Møl}} \rangle (Y^2 - Y_{\text{eq}}^2) \tag{4.11}$$

because $\tilde{s} \propto a^{-3}$. Plugging in the expressions Eq. 3.12 and Eq. 3.13 for H and $\tilde{s}$ in terms of effective degrees of freedom gives the form of the differential equation which will be implemented in the code for the numerical calculation of the relic density:

$$\begin{aligned} \frac{\mathrm{d}Y}{\mathrm{d}x} &= -\sqrt{\frac{45\pi}{G}} \frac{\sqrt{g_*} m}{x^2} \langle \sigma v_{\text{Møl}} \rangle (Y^2 - Y_{\text{eq}}^2) \\ \text{with } \sqrt{g_*} &= \frac{h_{\text{eff}}}{\sqrt{g_{\text{eff}}}} \left(\frac{T}{3} \frac{\mathrm{d} \ln h_{\text{eff}}}{\mathrm{d}T} \right) . \end{aligned} \tag{4.12}$$

4.3 Simplifying the thermal averages

The final, model-independent steps in rewriting the differential equation are the thermal averages of the equilibrium distributions as well as the thermally averaged cross section times velocity $\langle \sigma v_{\text{Møl}} \rangle$.
As mentioned above, the freeze-out happens at around $x = 20$. For $x \leq 1$ the interaction rate $n \langle \sigma v_{\text{Møl}} \rangle$ is usually so large that $n = n_{\text{eq}}$. This is also the initial condition when solving the differential equation numerically.
So the region of the differential equation that needs to be solved numerically fulfills $m \gtrsim T$

where the Fermi-Dirac distribution are well approximated as a Maxwell-Boltzmann distribution which simplifies the integrals.
With this approximation, the number density in equilibrium is

$$\begin{aligned} n_{\mathrm{eq}}(T) &= \frac{g}{(2\pi)^3}\int \mathrm{d}^3p \exp\left(\frac{-E}{T}\right) = \frac{g}{2\pi^2}\int_0^\infty \mathrm{d}p\, p^2 \exp\left(\frac{-\sqrt{p^2+m^2}}{T}\right) \\ &\overset{q^2=p^2/m^2+1}{=} \frac{gm^3}{2\pi^2}\int_1^\infty \mathrm{d}q\sqrt{q^2-1}\exp\left(-\frac{mq}{T}\right) \\ &= \frac{gm^3}{(6\pi^2}\sqrt{q^2-1}^3\exp\left(-xq\right)\Big|_{q=1}^{q=\infty} + \frac{gm^3}{6\pi^2}\frac{m}{T}\int_1^\infty \mathrm{d}q\sqrt{q^2-1}^3\exp\left(-\frac{mq}{T}\right) \\ &= \frac{gm^3}{6\pi^2}\frac{m}{T}\int_1^\infty \mathrm{d}q\sqrt{q^2-1}^3\exp\left(-\frac{mq}{T}\right) = \frac{g}{2\pi^2}m^2T\mathrm{K}_2\left(\frac{m}{T}\right)\,. \end{aligned} \tag{4.13}$$

The last line follows from the integral form of the modified Bessel functions of the second kind [16]

$$\mathrm{K}_n(z) = \frac{\sqrt{\pi}}{(n-\frac{1}{2})!}\left(\frac{z}{2}\right)^n\int_1^\infty \mathrm{d}u\exp(-zu)\left(u^2-1\right)^{n-1/2}\,. \tag{4.14}$$

$\langle\sigma v_{\mathrm{Møl}}\rangle$ of Eq. 4.5 can be written as a single integral. The first step toward this goal is writing

$$\mathrm{d}n_1^{\mathrm{eq}}\,\mathrm{d}n_2^{\mathrm{eq}} = \frac{g}{(2\pi)^3}\exp\left(\frac{-E_1}{T}\right)\mathrm{d}^3p_1\frac{g}{(2\pi)^3}\exp\left(\frac{-E_2}{T}\right)\mathrm{d}^3p_2 \tag{4.15}$$

in the numerator. The denominator of Eq. 4.5 has been calculated already as Eq. 4.13.
Total cross sections σ only depend on the total energy $\sqrt{s}$ in the center-of-mass system while $v_{\mathrm{Møl}}$ depends on the angle ϑ between the momenta of the particles as well as the magnitudes of those momenta $\vec{p_1}$ and $\vec{p_2}$. So by using spherical coordinates with three additional, independent angular coordinates to ϑ the phase space element becomes

$$\mathrm{d}^3p_1\,\mathrm{d}^3p_2 = 4\pi p_1^2\,\mathrm{d}p_1 4\pi p_2^2\,\mathrm{d}p_2\frac{1}{2}\,\mathrm{d}\cos\vartheta \tag{4.16}$$

As the Boltzmann factor depends on energy, but not on momentum, having the energies as the integration variables is more convenient. This leads to

$$\mathrm{d}^3p_1\,\mathrm{d}^3p_2 = 4\pi p_1E_1\,\mathrm{d}E_1 4\pi p_2E_2\,\mathrm{d}E_2\frac{1}{2}\,\mathrm{d}\cos\vartheta\,, \tag{4.17}$$

with the integration region in the numerator of Eq. 4.5 now being $E_1, E_2 \geq m$ and $|\cos\vartheta| \leq 1$.
The final transformation of integration variables is to the variables

$$E_+ = E_1 + E_2,\ E_- = E_1 - E_2 \text{ and } s = (p_{1,\mu}+p_{2,\mu})(p_1^\mu + p_2^\mu)\,. \tag{4.18}$$

For these variables, the integration boundaries are no longer independent. Since the energy in the center-of-mass frame

$$s = (E_1 + E_2)^2 - (\vec{p_1} + \vec{p_2})^2 = E_+^2 - (\vec{p_1} + \vec{p_2})^2 = 2m^2 + 2E_1E_2 - 2\vec{p_1}\vec{p_2}\cos\vartheta \tag{4.19}$$

is minimal for particles at rest with $\vec{p_1} = \vec{p_2} = 0$, which implies $E_1 = E_2 = m$ and thus $s = 4m^2$ and has no upper bound, the integration region for s is $s \geq 4m^2$.
$(\vec{p_1} + \vec{p_2})^2$ is ≥ 0 and so the integration region for E_+ then has to be $E_+ \geq \sqrt{s}$. Finally, the boundaries for E_- are given by the edge cases $|\cos\vartheta| = 1$. Solving this condition for E_- gives the integration boundaries

$$|E_-| = \sqrt{1 - \frac{4m^2}{s}}\sqrt{E_+^2 - s} \equiv \mathcal{E}\,. \tag{4.20}$$

The Jacobi determinant for the transformation $(E_1, E_2, \cos\vartheta) \to (E_+, E_-, s)$ is

$$\det T = -\frac{1}{4p_1p_2} \tag{4.21}$$

which results in the final momentum phase space element being

$$\mathrm{d}^3p_1\,\mathrm{d}^3p_2 = 2\pi^2 E_1E_2\,\mathrm{d}E_-\,\mathrm{d}E_+\,\mathrm{d}s\,. \tag{4.22}$$

Overall, the numerator of $\langle\sigma v_{\mathrm{M\o l}}\rangle$ can now be written as

$$\int \mathrm{d}n_1^{\mathrm{eq}}\,\mathrm{d}n_2^{\mathrm{eq}}\,\sigma v_{\mathrm{M\o l}} = 2\pi^2\frac{g^2}{(2\pi)^6}\int_{4m^2}^{\infty}\mathrm{d}s\sigma v_{\mathrm{M\o l}}E_1E_2\int_{\sqrt{s}}^{\infty}\mathrm{d}E_+\exp(-\frac{E_+}{T})\int_{-\mathcal{E}}^{\mathcal{E}}\mathrm{d}E_-\,. \tag{4.23}$$

The factor $\sigma v_{\mathrm{M\o l}}E_1E_2$ depends on s only:

$$\sigma v_{\mathrm{M\o l}}E_1E_2 = \frac{\sigma}{2}\sqrt{s(s-4m^2)}\,. \tag{4.24}$$

The above equation follows from substituting $\vec{v}_{1,2} = \vec{p}_{1,2}/E_{1,2}$ in the definition of $v_{\mathrm{M\o l}}$ Eq. 4.6 and using Eq. 4.19 for s. With this, both the E_- and E_+ integrals can be evaluated to give

$$\begin{aligned}\int \mathrm{d}n_1^{\mathrm{eq}}\,\mathrm{d}n_2^{\mathrm{eq}}\,\sigma v_{\mathrm{M\o l}} &= \frac{g^2}{32\pi^4}\int_{4m^2}^{\infty}\mathrm{d}s\sigma\sqrt{s(s-4m^2)}\int_{\sqrt{s}}^{\infty}\mathrm{d}E_+\exp(-\frac{E_+}{T})\mathcal{E}\\ &= \frac{g^2}{32\pi^4}\int_{4m^2}^{\infty}\mathrm{d}s\sigma(s-4m^2)\int_{\sqrt{s}}^{\infty}\mathrm{d}E_+\exp(-\frac{E_+}{T})\sqrt{E_+^2-s}\\ &= \frac{g^2}{32\pi^4}T\int_{4m^2}^{\infty}\mathrm{d}s\sigma(s-4m^2)\sqrt{s}\mathrm{K}_1\left(\frac{\sqrt{s}}{T}\right)\,,\end{aligned} \tag{4.25}$$

where the last line follows from the substitution $u = E_+/\sqrt{s}$ and the form for K_1 given in Eq. 4.14. With this, the final result for $\langle \sigma v_{\mathrm{Møl}} \rangle$ becomes

$$\langle \sigma v_{\mathrm{Møl}} \rangle = \frac{1}{8m^4 T \mathrm{K}_2^2(m/T)} \int_{4m^2}^{\infty} \sigma(s - 4m^2)\sqrt{s}\mathrm{K}_1(\sqrt{s}/T)\,\mathrm{d}s\,. \tag{4.26}$$

5 Annihilation Cross Sections and Decay Widths of the Dark Matter Model

In order to solve the Boltzmann equation and then obtain the relic density, what remains to be done is the calculation of the unpolarized total cross section σ appearing in the thermally averaged cross section times velocity $\langle \sigma v_{\text{Møl}} \rangle$ and thus the Boltzmann equations. Furthermore, the decay width of the scalar ϕ is needed to make use of the restriction Eq. 3.15 and will also prove useful in calculating the cross sections.

These calculations are easiest to perform using Feynman diagrams and Feynman rules. They are explained in detail in Appendix Ax. In short, they provide a straightforward way to calculate the matrix element $\langle f|U|i\rangle = \mathcal{M}_{\text{fi}}$ relevant for the differential cross section and the decay width by giving mathematical expressions to incoming and outgoing particles as well as virtual particles mediating the process, called propagators, and the interactions points between particles, commonly called vertices. U is the time evolution operator and $|i\rangle(|f\rangle)$ is the initial (final) state. The connection between these matrix elements, decay widths and differential cross sections is described in chapter 4.5 of [17].

This chapter only considers the leading order of the processes corresponding to the simplest Feynman diagrams. For large couplings, higher order corrections from more complex diagrams become relevant. Their calculation are out of the scope of this thesis.

In the only case of both two ingoing and two outgoing particles dealt with in this thesis, the unpolarized differential cross section in the center-of-mass frame is given as

$$\frac{\mathrm{d}\sigma}{\mathrm{d}\Omega} = \frac{\alpha}{64\pi^2 s}\frac{|\vec{p_{\text{f}}}|}{|\vec{p_{\text{i}}}|}\overline{|\mathcal{M}|}^2\,, \tag{5.1}$$

where s is again the square of the total energy, $\vec{p_{\text{i}}}$ the momentum of the initial particles and $\vec{p_{\text{f}}}$ the momentum of the outgoing particles. α is only relevant if the two outgoing particles are identical. Then there is $\alpha = 1/2$ to prevent double counting.

The unpolarized differential decay width for a decay into two particles in the center-of-mass frame is

$$\mathrm{d}\Gamma = \alpha\frac{|\vec{p_{\text{f}}}|}{32\pi^2 m_{\text{A}^2}}\overline{|\mathcal{M}|}^2\,\mathrm{d}\Omega\,. \tag{5.2}$$

m_{A} is the mass of the decaying particle.

$\overline{|\mathcal{M}|}^2$, often referred to as the invariant amplitude, is defined as the sum over all possible

final states and the average over all possible initial states of $|\mathcal{M}_{\mathrm{fi}}|^2$. For initial as well as final states these possible states are the spin states of the particles and thus

$$\overline{|\mathcal{M}|}^2 = \sum_{\mathrm{i}} \frac{1}{2S_{\mathrm{i}}+1} \sum_{f} |\mathcal{M}_{\mathrm{fi}}|^2 \,, \tag{5.3}$$

where S_{i} is the spin of the incoming particles [17, p. 132]. In principle, these spin states could be measured which is why $\overline{|\mathcal{M}|}^2$ is also known as the unpolarized squared matrix element and consequently the derived decay width or cross section is also unpolarized.
For the purposes of describing dark matter freeze-out, these unpolarized formulas are the only ones of interest [15, p. 150]. The expressions obtained for $\mathcal{M}$ from the Feynman rules and especially $\overline{|\mathcal{M}|}^2$ contain a number of Dirac matrices γ^μ. Specifically, the summation for $\overline{|\mathcal{M}|}^2$ leads to a trace over a product of Dirac matrices. For this reason, Appendix B contains some useful identities for these matrices.

5.1 Mandelstam variables

Before calculating the invariant amplitudes it is useful to introduce some Lorentz invariant variables with which these can be expressed instead of using variables such as scattering angles which are dependent on the frame of reference. The most common choice are known as the Mandelstam variables.
From here on p_{A} and p_{B} will denote the four-momenta of particles in the initial state while k_1 and k_2 will refer to the four-momenta of the particles in the final state. Squared four-momenta as well as products of them refer to relativistic dot products: $p^2 = p_0 p_0 - p_{\mathrm{j}} p_{\mathrm{j}}$ and $pk = p_\mu k^\mu$. Three-momenta are indicated as $\vec{p}$.
The first of the Mandelstam variables is the square of the total energy in the center-of-mass frame

$$s \equiv (p_{\mathrm{A}} + p_{\mathrm{B}})^2 = (k_1 + k_2)^2 \,. \tag{5.4}$$

The other two are useful to compactly denote the angular dependencies in the differential cross sections

$$\begin{aligned} t &\equiv (p_{\mathrm{A}} - k_1)^2 = (k_2 - p_{\mathrm{B}})^2 \\ u &\equiv (p_{\mathrm{B}} - k_2)^2 = (k_1 - p_{\mathrm{A}})^2 \,. \end{aligned} \tag{5.5}$$

Because of conservation of energy the three Mandelstam variables are not independent but fulfill the relation [17, p. 158]

$$s + t + u = m_{\mathrm{A}}^2 + m_{\mathrm{B}}^2 + m_1^2 + m_2^2 \,. \tag{5.6}$$

It will prove useful to have a differential cross section in terms of t instead of the scattering angle ϑ. Since t as a function of the scattering angle ϑ and s is

$$t = m_{\mathrm{A}}^2 + m_1^2 - 2E_{\mathrm{A}}E_1 + 2|\vec{p_{\mathrm{A}}}||\vec{p_1}|\cos\vartheta \tag{5.7}$$

this has the form

$$\frac{\mathrm{d}\sigma}{\mathrm{d}t} = \frac{1}{64\pi s|\vec{p_{\mathrm{i}}}|^2}\overline{|\mathcal{M}|}^2 \tag{5.8}$$

where the integral over the azimuthal angle has already been performed to give a factor of 2π [18].

5.2 Decay width of the scalar portal

The decay width Γ of the scalar ϕ is easier to calculate than the cross sections as the Feynman diagram does not include a propagator and only has one vertex. The calculation will be done for the decay $\phi \to \nu\bar{\nu}$ first. From there, the calculation of the decay width for $\phi \to D\bar{D}$ will only be a matter of replacing $m_\nu \to m_{\mathrm{D}}$, $g_{\mathrm{n}} \to g_{\mathrm{x}}$ and $g'_{\mathrm{n}} \to g'_{\mathrm{x}}$.

5.2.1 Decay width for the decay $\phi \to \nu\bar{\nu}$

By the Feynman rules introduced in Appendix A, the matrix element for the process $\phi \to \nu\bar{\nu}$ where ν and $\bar{\nu}$ are a neutrino and an anti-neutrino of the same flavor has the form [4]

$$\mathcal{M} = \bar{u}^{\mathrm{s}_1}(k_1)(-\hat{\imath}(g_{\mathrm{n}} + \hat{\imath}g'_{\mathrm{n}}\gamma^5))v^{\mathrm{s}_2}(k_2)\,. \tag{5.9}$$

This process is illustrated on the right in Fig. 5.1. The factor in the middle represents the vertex, while $\bar{u}^{\mathrm{s}_1}(k_1)$ is for the outgoing neutrino and $v^{\mathrm{s}_2}(k_2)$ for the anti-neutrino. The scalar corresponds to a factor of 1 and hence changes nothing.

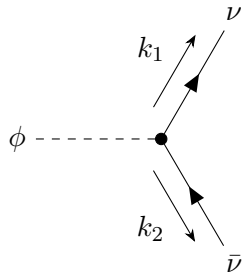

Figure 5.1: Feynman diagram of the decay $\phi \to \nu\bar{\nu}$.

To calculate the invariant amplitude, the complex conjugate $\mathcal{M}^*$ is needed. As $\mathcal{M}$ is just a number, this is the same as the hermitian conjugate $\mathcal{M}^\dagger$ which is

$$\mathcal{M}^\dagger = \bar{v}^{\mathrm{s}_2}(k_2)(\hat{\imath}(g_{\mathrm{n}} + \hat{\imath}g'_{\mathrm{n}}\gamma^5))u^{\mathrm{s}_1}(k_1)\,. \tag{5.10}$$

[4] Some textbooks such as [17] define $\mathcal{M}$ so that an additional factor $\hat{\imath}$ would have to appear in front of $\mathcal{M}$ here while others such as [6] do not. This thesis omits the additional factor $\hat{\imath}$.

This follows from the identities Eq. B.2 and Eq. B.4 as well as

$$(AB)^\dagger = B^\dagger A^\dagger \,, \tag{5.11}$$

which holds for any two matrices A and B.
For the decay width, the object of interest is the squared absolute value of $\mathcal{M}$

$$|\mathcal{M}|^2 = \mathcal{M}\mathcal{M}^\dagger = \left\{\bar{u}^{s_1}(k_1)(-\hat{\imath}(g_\mathrm{n} + \hat{\imath}g'_\mathrm{n}\gamma^5))v^{s_2}(k_2)\right\}\left\{\bar{v}^{s_2}(k_2)(\hat{\imath}(g_\mathrm{n} + \hat{\imath}g'_\mathrm{n}\gamma^5))u^{s_1}(k_1)\right\} \,. \tag{5.12}$$

This still depends on the spin states of the outgoing neutrinos which are irrelevant for the purposes of this thesis. Using Feynman slash notation, where $\not{Q} = \gamma^\mu Q_\mu$ is used for compactness, the sum over the spins gives

$$\begin{aligned}
\overline{|\mathcal{M}|}^2 &= \sum_{s_1,\,s_2} \mathcal{M}\mathcal{M}^\dagger \\
&= \sum_{s_1,\,s_2} \sum_{A,B,C,D=1}^{4} \bar{u}^{s_1}_\mathrm{A}(k_1)(-\hat{\imath}(g_\mathrm{n}\mathbb{1}_\mathrm{AB} + \hat{\imath}g'_\mathrm{n}{\gamma^5}_\mathrm{AB}))v^{s_2}_\mathrm{B}(k_2)\bar{v}^{s_2}_\mathrm{C}(k_2)(\hat{\imath}(g_\mathrm{n}\mathbb{1}_\mathrm{CD} + \hat{\imath}g'_\mathrm{n}{\gamma^5}_\mathrm{CD}))u^{s_1}_\mathrm{D}(k_1) \\
&= \sum_{s_1,\,s_2} \sum_{A,B,C,D=1}^{4} u^{s_1}_\mathrm{D}(k_1)\bar{u}^{s_1}_\mathrm{A}(k_1)(-\hat{\imath}(g_\mathrm{n}\mathbb{1}_\mathrm{AB} + \hat{\imath}g'_\mathrm{n}{\gamma^5}_\mathrm{AB}))v^{s_2}_\mathrm{B}(k_2)\bar{v}^{s_2}_\mathrm{C}(k_2)(\hat{\imath}(g_\mathrm{n}\mathbb{1}_\mathrm{CD} + \hat{\imath}g'_\mathrm{n}{\gamma^5}_\mathrm{CD})) \\
&= \mathrm{Tr}\left\{(\not{k}_1 + m_\nu)(-\hat{\imath}(g_\mathrm{n} + \hat{\imath}g'_\mathrm{n}\gamma^5))\,(\not{k}_2 - m_\nu)\hat{\imath}(g_\mathrm{n} + \hat{\imath}g'_\mathrm{n}\gamma^5)\right\}
\end{aligned} \tag{5.13}$$

by making use of the completeness relations Eq. A.5 in the last line. As an intermediate step, the second line of Eq. 5.13 writes out the matrix multiplication explicitly which allows the entries of the matrices to be moved freely. The order of the third line then enables the use of the completeness relations.
So what needs to be calculated is the trace of a product of Dirac matrices. As mentioned in the previous section, this is the case for invariant amplitudes of all processes. Appendix B contains the identities used in the following steps to simplify the above form of the invariant amplitude.
One of these is that the trace over any term with an uneven number of Dirac matrices vanishes. Hence, the expansion

$$\overline{|\mathcal{M}|}^2 = \mathrm{Tr}\left\{\not{k}_1(-\hat{\imath}(g_\mathrm{n} + \hat{\imath}g'_\mathrm{n}\gamma^5))\,\not{k}_2\hat{\imath}(g_\mathrm{n} + \hat{\imath}g'_\mathrm{n}\gamma^5)\right\} - \mathrm{Tr}\left\{m_\nu(-\hat{\imath}(g_\mathrm{n} + \hat{\imath}g'_\mathrm{n}\gamma^5))\,m_\nu\hat{\imath}(g_\mathrm{n} + \hat{\imath}g'_\mathrm{n}\gamma^5)\right\} \tag{5.14}$$

of the invariant amplitude holds. As ${\gamma^5}^2 = \mathbb{1}$, this becomes

$$\overline{|\mathcal{M}|}^2 = \mathrm{Tr}\left(g_\mathrm{n}^2\not{k}_1\not{k}_2\right) - \mathrm{Tr}\left({g'_\mathrm{n}}^2\not{k}_1\gamma^5\not{k}_2\gamma^5\right) + \mathrm{Tr}\left({g'_\mathrm{n}}^2 m_\nu\gamma^5 m_\nu\gamma^5\right) - \mathrm{Tr}\left(g_\mathrm{n}^2 m_\nu^2\right) \tag{5.15}$$

which leads to

$$\overline{|\mathcal{M}|}^2 = 4\left(g_\mathrm{n}^2 + {g'_\mathrm{n}}^2\right)\, k_1 k_2 + 4\left({g'_\mathrm{n}}^2 - g_\mathrm{n}^2\right) m_\nu^2 \tag{5.16}$$

because of $\{\gamma_\mu, \gamma^5\} = 0$ and the identity Eq. B.6 for the trace over a product of two Dirac matrices. This can be written in terms of s with equation Eq. 5.4

$$\overline{|\mathcal{M}|}^2 = 4\left(g_\mathrm{n}^2 + {g'_\mathrm{n}}^2\right)\, \left(\frac{s}{2} - m_\nu^2\right) + 4\left({g'_\mathrm{n}}^2 - g_\mathrm{n}^2\right) m_\nu^2 \,. \tag{5.17}$$

Here, the center-of-mass energy is $\sqrt{s} = m_\phi$ and the mass of the neutrinos is negligible against all relevant masses of ϕ. Therefore, the final form of the invariant amplitude is

$$\overline{|\mathcal{M}|}^2 = 2\left(g_\mathrm{n}^2 + {g'_\mathrm{n}}^2\right)\, m_\phi^2 \,. \tag{5.18}$$

Putting this in the formula for the decay width Eq. 5.2, with $\alpha = 1$ because ν and $\bar{\nu}$ are not identical particles, gives

$$\begin{aligned} \Gamma_{\phi\to\nu\bar{\nu}} &= \frac{|\vec{k_1}|}{32\pi^2 m_\phi^2} \cdot \int \overline{|\mathcal{M}|}^2 \mathrm{d}\Omega \\ &= \frac{\frac{m_\phi}{2}}{32\pi^2 m_\phi^2} 3 \cdot 2\left(g_\mathrm{n}^2 + {g'_\mathrm{n}}^2\right) m_\phi^2 \cdot 4\pi \\ &= \frac{3}{8\pi}\left(g_\mathrm{n}^2 + {g'_\mathrm{n}}^2\right) m_\phi \,, \end{aligned} \tag{5.19}$$

The additional factor of 3 comes from the three neutrino flavors which each contribute the same invariant amplitude of Eq. 5.18 to the decay width as the mass of the neutrinos can be neglected.

The only case that will be considered in the numerical analysis is $g_\mathrm{n} = g'_\mathrm{n}$ in which case

$$\Gamma_{\phi\to\nu\bar{\nu}} = \frac{3}{4\pi}\, g_\mathrm{n}^2\, m_\phi \tag{5.20}$$

is the simplest form for the decay width. To avoid an impact of this decay on the Big Bang nucleosynthesis, it should be

$$\begin{aligned} &\frac{1}{\Gamma_{\phi\to\nu\bar{\nu}}} < 1\,\mathrm{s} \\ \Leftrightarrow\ & g_\mathrm{n}\sqrt{\frac{m_\phi}{\mathrm{GeV}}} > \sqrt{\frac{4\pi}{3}\frac{\hbar}{1\,\mathrm{s}\cdot\mathrm{GeV}}} = 1.6604 \cdot 10^{-12} \,. \end{aligned} \tag{5.21}$$

5.2.2 Decay width for the decay $\phi \to D\bar{D}$

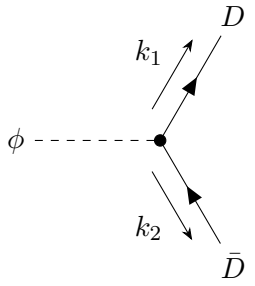

Figure 5.2: Feynman diagram of the decay $\phi \to D\bar{D}$.

Calculating the matrix element for the decay $\phi \to D\bar{D}$ which is illustrated in Fig. 5.2 with the Feynman rules from Appendix A gives

$$\mathcal{M} = \bar{u}^{s_1}(k_1)(-\hat{\imath}(g_\mathrm{x} + \hat{\imath} g'_\mathrm{x}\gamma^5))v^{s_2}(k_2)\,. \tag{5.22}$$

This is the same as Eq. 5.9 with the replacements $g_\mathrm{n} \to g_\mathrm{x}$ and $g'_\mathrm{n} \to g'_\mathrm{x}$. So the invariant amplitude will be that of Eq. 5.17 with the additional replacement $m_\nu \to m_\mathrm{D}$. Hence, the decay width Eq. 5.2 is

$$\begin{aligned}\Gamma_{\phi\to D\overline{D}} &= \frac{|\vec{k_1}|}{32\pi^2 m_\phi^2} \cdot \int \overline{|\mathcal{M}|}^2 \mathrm{d}\Omega \\ &= \frac{\sqrt{\frac{m_\phi^2}{4} - m_\mathrm{D}^2}}{8\pi m_\phi^2} \cdot \left[4\left(g_\mathrm{x}^2 + {g'_\mathrm{x}}^2\right)\frac{m_\phi^2}{2} - 8 g_\mathrm{x}^2 m_\mathrm{D}^2\right]\end{aligned} \tag{5.23}$$

and in the case of $g_\mathrm{x} = g'_\mathrm{x}$ it simplifies to

$$\Gamma_{\phi\to D\overline{D}} = \frac{g_\mathrm{x}^2}{4\pi} m_\phi \left(1 - \frac{2m_\mathrm{D}^2}{m_\phi^2}\right)\sqrt{1 - \frac{4m_\mathrm{D}^2}{m_\phi^2}}\,. \tag{5.24}$$

This decay is only possible for $m_\phi \geq 2m_\mathrm{D}$ because of conservation of energy. However, this region of the parameter space cannot be investigated with the approach outlined in Chapter 4 as this decay would be a source of additional D. Investigating this part of the parameter space would therefore require coupled differential equations for ϕ and D.

5.3 Cross section of $D\bar{D} \to \nu\bar{\nu}$

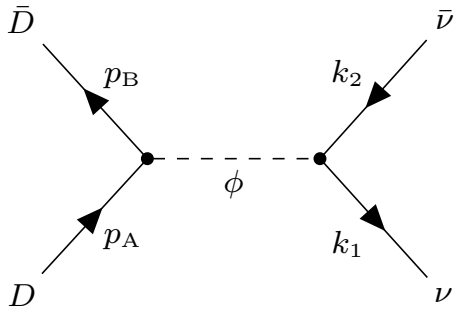

Figure 5.3: The only Feynman diagram for the annihilation process $D\bar{D} \to \nu\bar{\nu}$ with two vertices.

The Feynman diagram for the annihilation process $D\bar{D} \to \nu\bar{\nu}$ can be seen in Fig. 5.3. Using the Feynman rules of Appendix A gives the matrix element

$$\begin{aligned}\mathcal{M} &= \text{"}D\text{ "fermion line"} \cdot \text{scalar propagator} \cdot \text{"}\nu\text{ fermion line"} \\ &= \left\{\bar{v}^{s_1}(p_B)(-\hat{\imath}(g_x + \hat{\imath}g'_x\gamma^5))u^{s_2}(p_A)\right\}\left(\frac{\hat{\imath}}{s - m_\phi^2 + \hat{\imath}\varepsilon}\right)\left\{\bar{u}^{s_3}(k_1)(-\hat{\imath}(g_n + \hat{\imath}g'_n\gamma^5))v^{s_4}(k_2)\right\} .\end{aligned} \tag{5.25}$$

Consequently, the matrix element is just the product of the matrix elements for the decays $\phi \to \nu\bar{\nu}$ and $\phi \to D\bar{D}$ with the additional term for the scalar propagator since the Feynman diagram is just the Feynman diagrams of both of these decays connected through the scalar propagator.

The scalar propagator has to carry a four-momentum with $q^2 = s$ by conservation of energy and momentum. Because of this, the propagator and thus the cross section diverges for $s \to m_\phi$ and $\varepsilon \to 0$ which does not make sense.

This process is in fact a case of a Breit-Wigner resonance, which occurs when a process $A + B \to C + D$ is mediated by an unstable particle O. Here, an additional term $\hat{\imath}m_O^2\Gamma_O$ needs to be included in the denominator of the propagator to obtain the correct result [6, pp. 461]. Γ_O is the total decay width of the particle O, that is, the sum over the decay widths for each possible decay channel

$$\Gamma_O = \sum_{x \geq y} \Gamma_{O \to x+y} \,. \tag{5.26}$$

In the case of $D\bar{D} \to \nu\bar{\nu}$, the unstable particle O is the scalar ϕ and the possible decay channels are $\phi \to \nu\bar{\nu}$ and $\phi \to D\bar{D}$ if $m_\phi \geq 2m_D$ and only $\phi \to \nu\bar{\nu}$ if $m_\phi < 2m_D$.

With this adjustment, the $\hat{\imath}\varepsilon-$terms preventing a divergence can be dropped and the hermitian conjugate of the matrix element is

$$\mathcal{M}^\dagger = \left\{\bar{u}^{s_2}(p_A)(\hat{\imath}(g_x + \hat{\imath}g'_x\gamma^5))v^{s_1}(p_B)\right\} \cdot \left(\frac{-\hat{\imath}}{s - m_\phi^2 - \hat{\imath}m_\phi\Gamma_\phi}\right) \cdot \left\{\bar{v}^{s_4}(k_2)(\hat{\imath}(g_n + \hat{\imath}g'_n\gamma^5))u^{s_3}(k_1)\right\} \tag{5.27}$$

because of the same identities used to obtain Eq. 5.10.
The unpolarized cross section depends on the invariant amplitude $\overline{|\mathcal{M}|}^2$ which is $|\mathcal{M}|^2$ averaged over initial spins and summed over final spins. This is

$$\begin{aligned}\overline{|\mathcal{M}|}^2 &= \frac{1}{4}\cdot\sum_{i=1}^{4}\sum_{s_i}\mathcal{M}\mathcal{M}^\dagger \equiv \frac{1}{4}\cdot\frac{1}{(s-m_\phi^2)^2+m_\phi^2\Gamma^2}\cdot \mathrm{Tr}\,\mathbb{B}\,\mathrm{Tr}\,\mathbb{A}\\ &= \frac{1}{4}\cdot\frac{1}{(s-m_\phi^2)^2+m_\phi^2\Gamma^2}\cdot \mathrm{Tr}\left\{(\not{p}_\mathrm{B}-m_\mathrm{D})(-\hat{\imath}(g_\mathrm{x}+\hat{\imath}g'_\mathrm{x}\gamma^5))(\not{p}_\mathrm{A}+m_\mathrm{D})(\hat{\imath}(g_\mathrm{x}+\hat{\imath}g'_\mathrm{x}\gamma^5))\right\}\\ &\quad\times \mathrm{Tr}\left\{(\not{k}_1+m_\nu)(-\hat{\imath}(g_\mathrm{n}+\hat{\imath}g'_\mathrm{n}\gamma^5))\,(\not{k}_2-m_\nu)\hat{\imath}(g_\mathrm{n}+\hat{\imath}g'_\mathrm{n}\gamma^5)\right\}\end{aligned} \tag{5.28}$$

because the terms in {...} are numbers and thus commute. Reordering them enables the use of the completeness relations of Eq. A.5 and leads to the traces in the same way that has been shown in Eq. 5.13.
Both $\mathrm{Tr}\,\mathbb{B}$ and $\mathrm{Tr}\,\mathbb{A}$ in the above equation have been calculated already, the first one for the decay width of $\phi\to D\bar{D}$ and the second one for the decay width of $\phi\to\nu\bar{\nu}$. Substituting these in results in

$$\overline{|\mathcal{M}|}^2 = \frac{3}{4(s-m_\phi^2)^2+4m_\phi^2\Gamma^2}\left[2\left(g_\mathrm{x}^2+{g'_\mathrm{x}}^2\right)s-8g_\mathrm{x}^2m_\mathrm{D}^2\right]\left[2\left(g_\mathrm{n}^2+{g'_\mathrm{n}}^2\right)s\right] \tag{5.29}$$

where the factor 3 again accounts for the three neutrino flavors and any terms containing the mass of any neutrino have been dropped.
Therefore, the differential cross section of Eq. 5.1 for this process is

$$\begin{aligned}\frac{\mathrm{d}\sigma_{D\bar{D}\to\nu\bar{\nu}}}{\mathrm{d}\Omega} &= \frac{1}{64\,\pi^2 s}\cdot\frac{|\vec{p_\mathrm{f}}|}{|\vec{p_\mathrm{i}}|}\overline{|\mathcal{M}|}^2\\ &= \frac{3}{256\pi^2}\frac{\left(g_\mathrm{n}^2+{g'_\mathrm{n}}^2\right)s\left[\left(g_\mathrm{x}^2+{g'_\mathrm{x}}^2\right)s-4g_\mathrm{x}^2m_\mathrm{D}^2\right]}{\sqrt{s\left(s-4m_\mathrm{D}^2\right)}\left((s-m_\phi^2)^2+m_\phi^2\Gamma^2\right)}\,.\end{aligned} \tag{5.30}$$

This just depends on s which is independent of the scattering angle in the center-of-mass frame and so the total cross section only includes an additional factor 4π:

$$\sigma_{D\bar{D}\to\nu\bar{\nu}} = \frac{3}{16\pi}\frac{\left(g_\mathrm{n}^2+{g'_\mathrm{n}}^2\right)s\left[\left(g_\mathrm{x}^2+{g'_\mathrm{x}}^2\right)s-4g_\mathrm{x}^2m_\mathrm{D}^2\right]}{\sqrt{s\left(s-4m_\mathrm{D}^2\right)}\left((s-m_\phi^2)^2+m_\phi^2\Gamma^2\right)} \tag{5.31}$$

In the case considered in the numerical solution to the Boltzmann equation of $g_\mathrm{n} = g'_\mathrm{n}$ and $g_\mathrm{x} = g'_\mathrm{x}$, this becomes

$$\sigma_{D\bar{D}\to\nu\bar{\nu}} = \frac{3}{4\,\pi} g_\mathrm{x}^2 g_\mathrm{n}^2 \frac{\sqrt{s}\,\left(s - 2m_\mathrm{D}^2\right)}{\sqrt{s - 4m_\mathrm{D}^2}\,\left[(s - m_\phi^2)^2 + m_\phi^2 \Gamma_\phi^2\right]}\,. \tag{5.32}$$

5.4 Cross section of $D\bar{D} \to \phi\phi$

There are two distinct Feynman diagrams for the annihilation process $D\bar{D} \to \phi\phi$ which are shown in Fig. 5.4. They are referred to as t-channel and u-channel respectively after the four-momentum q^2 the propagator carries. These are physically indistinguishable as the outgoing scalars ϕ are identical particles. So the matrix element for the cross section will be given by the sum of t- and u-channel matrix elements:

$$\mathcal{M} = \mathcal{M}_\mathrm{t} + \mathcal{M}_\mathrm{u}\,. \tag{5.33}$$

This means, that the invariant amplitude

$$\overline{|\mathcal{M}|}^2 = \overline{|\mathcal{M}_t + \mathcal{M}_u|^2} = \overline{|\mathcal{M}_\mathrm{t}|}^2 + \overline{|\mathcal{M}_\mathrm{u}|}^2 + \overline{\mathcal{M}_\mathrm{t}\mathcal{M}_\mathrm{u}^\dagger} + \overline{\mathcal{M}_\mathrm{u}\mathcal{M}_\mathrm{t}^\dagger} \tag{5.34}$$

contains an interference term between the two channels in addition to the invariant amplitudes of both channels.

Because of this, it is useful to work with a generic matrix element $\mathcal{M}_\mathrm{y}$ where the index $y = 1$ refers to the matrix element with four-momentum of the propagator of $q_1^2 = t$ and $y = 2$

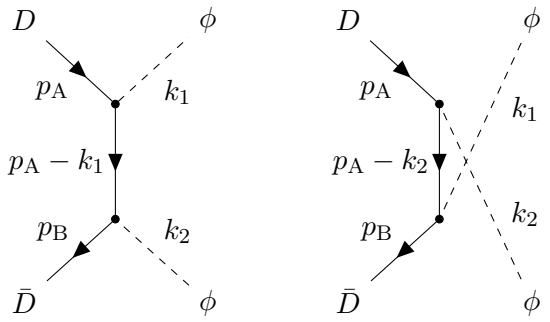

Figure 5.4: The two Feynman diagrams for the annihilation process $D\bar{D} \to \phi\phi$ with two vertices. The crossed scalar lines in the diagram on the right just serve as an illustration that the momenta of the scalars are switched compared to the diagram on the left - there is no self-interaction between the scalars happening.

refers to the matrix element with four-momentum of the propagator of $q_2^2 = u$.
According to the Feynman rules of Appendix A, the matrix element is

$$\mathcal{M}_\mathrm{y} = \bar{v}^{s_2}(p_\mathrm{B}) \left(-\hat{\imath}(g_\mathrm{x} + \hat{\imath} g'_\mathrm{x} \gamma^5)\right) \cdot \left(\hat{\imath} \frac{\not{q}_\mathrm{y} + m_\mathrm{D}}{{q_\mathrm{y}}^2 - m_\mathrm{D}^2 + \hat{\imath}\varepsilon}\right) \cdot \left(-\hat{\imath}(g_\mathrm{x} + \hat{\imath} g'_\mathrm{x} \gamma^5)\right) u^{s_1}(p_\mathrm{A}) \,. \tag{5.35}$$

The complex conjugate of the matrix element is

$$\mathcal{M}_\mathrm{y}{}^\dagger = \bar{u}^{s_1}(p_\mathrm{A}) \hat{\imath}(g_\mathrm{x} + \hat{\imath} g'_\mathrm{x} \gamma^5) \cdot \left(-\hat{\imath} \frac{\not{q}_\mathrm{y} + m_\mathrm{D}}{{q_\mathrm{y}}^2 - m_\mathrm{D}^2 + \hat{\imath}\varepsilon}\right) \cdot \hat{\imath}(g_\mathrm{x} + \hat{\imath} g'_\mathrm{x} \gamma^5) v^{s_2}(p_\mathrm{B}) \tag{5.36}$$

because of the same identities outlined in section 5.2.1 to obtain Eq. 5.10.
Therefore, the general summand of the invariant amplitude becomes

$$\begin{aligned}
\overline{\mathcal{M}_\mathrm{y} \mathcal{M}_\mathrm{z}{}^\dagger} &= \frac{1}{4} \sum_{s_1, s_2 = 1}^{2} \mathcal{M}_\mathrm{y} \mathcal{M}_\mathrm{z}{}^\dagger \\
&= \frac{1}{4\left(q_\mathrm{y}^2 - m_\mathrm{D}^2 + \hat{\imath}\varepsilon\right)\left(q_\mathrm{z}^2 - m_\mathrm{D}^2 - \hat{\imath}\varepsilon\right)} \cdot \mathrm{Tr}\Big\{ \left(\not{p}_\mathrm{A} + m_\mathrm{D}\right) (g_\mathrm{x} + \hat{\imath} g'_\mathrm{x} \gamma^5) \left(\not{q}_\mathrm{y} + m_\mathrm{D}\right) \\
&\quad \times (g_\mathrm{x} + \hat{\imath} g'_\mathrm{x} \gamma^5) \left(\not{p}_\mathrm{B} - m_\mathrm{D}\right) (g_\mathrm{x} + \hat{\imath} g'_\mathrm{x} \gamma^5) \left(\not{q}_\mathrm{z} + m_\mathrm{D}\right) (g_\mathrm{x} + \hat{\imath} g'_\mathrm{x} \gamma^5) \Big\} \,. \\
&\equiv \frac{\mathrm{Tr}\, \mathbb{A}_{yz}}{4\left(q_\mathrm{y}^2 - m_\mathrm{D}^2 + \hat{\imath}\varepsilon\right)\left(q_\mathrm{z}^2 - m_\mathrm{D}^2 - \hat{\imath}\varepsilon\right)} \,.
\end{aligned} \tag{5.37}$$

The trace over the matrix $\mathbb{A}_{yz}$ can be obtained by the same completeness relations Eq. A.5 used to obtain the traces in the three previous sections.
$\mathrm{Tr}\, \mathbb{A}_{yz}$ can be expanded to a sum of terms containing traces over two and four Dirac matrices by first using ${\gamma^5}^2 = \mathbb{1}$ and $\{\gamma_\mu, \gamma^5\} = 0$ to obtain

$$\begin{aligned}
\mathrm{Tr}\, \mathbb{A}_{yz} = \ & \mathrm{Tr}\Big\{ \left(\not{p}_\mathrm{A} + m_\mathrm{D}\right) \left[\not{q}_\mathrm{y} (g_\mathrm{x}^2 + {g'_\mathrm{x}}^2) + m(g_\mathrm{x}^2 - {g'_\mathrm{x}}^2 + 2\hat{\imath} g_\mathrm{x} g'_\mathrm{x} \gamma^5)\right] \\
& \times \left(\not{p}_\mathrm{B} - m_\mathrm{D}\right) \left[\not{q}_\mathrm{z} (g_\mathrm{x}^2 + {g'_\mathrm{x}}^2) + m(g_\mathrm{x}^2 - {g'_\mathrm{x}}^2 + 2\hat{\imath} g_\mathrm{x} g'_\mathrm{x} \gamma^5)\right] \Big\}
\end{aligned} \tag{5.38}$$

and then $\mathrm{Tr}(\gamma_\mu \gamma_\mu \gamma^5) = 0$ as well as the fact that the trace of an uneven number of Dirac matrices vanishes lead to

$$\begin{aligned}
\mathrm{Tr}\, \mathbb{A}_{yz} = \ & (g_\mathrm{x}^2 + {g'_\mathrm{x}}^2)^2 \,\mathrm{Tr}\left[\not{p}_\mathrm{A} \not{q}_\mathrm{y} \not{p}_\mathrm{B} \not{q}_\mathrm{z}\right] + m_\mathrm{D}^2 (g_\mathrm{x}^4 - {g'_\mathrm{x}}^4)\, \mathrm{Tr}\left[\not{p}_\mathrm{B} \not{q}_\mathrm{y} + \not{p}_\mathrm{B} \not{q}_\mathrm{z} - \not{p}_\mathrm{A} \not{q}_\mathrm{y} - \not{p}_\mathrm{A} \not{q}_\mathrm{z}\right] \\
& + m_\mathrm{D}^2 (g_\mathrm{x}^2 + {g'_\mathrm{x}}^2)^2 \,\mathrm{Tr}\left[\not{p}_\mathrm{A} \not{p}_\mathrm{B} - \not{q}_\mathrm{y} \not{q}_\mathrm{z}\right] - 4 m_\mathrm{D}^4 \left((g_\mathrm{x}^2 - {g'_\mathrm{x}}^2)^2 - 4 g_\mathrm{x}^2 {g'_\mathrm{x}}^2\right) \,.
\end{aligned} \tag{5.39}$$

With the identities Eq. B.7 for the trace over four Dirac matrices and Eq. B.6 for the trace over two Dirac matrices this becomes

$$\begin{aligned}\operatorname{Tr}\mathbb{A}_{yz} = {} & 4(g_{\mathrm{x}}^2 + g_{\mathrm{x}}'^2)^2 \left[(p_{\mathrm{A}}q_{\mathrm{y}})(p_{\mathrm{B}}q_{\mathrm{z}}) + (p_{\mathrm{A}}q_{\mathrm{z}})(p_{\mathrm{B}}q_{\mathrm{y}}) - (p_{\mathrm{A}}p_{\mathrm{B}})(q_{\mathrm{y}}q_{\mathrm{z}}) + m_{\mathrm{D}}^2(p_{\mathrm{A}}p_{\mathrm{B}} - q_{\mathrm{y}}q_{\mathrm{z}})\right] \\ & - 4m_{\mathrm{D}}^4 \left(g_{\mathrm{x}}^4 + g_{\mathrm{x}}'^4 - 6g_{\mathrm{x}}^2 g_{\mathrm{x}}'^2\right) + 4m_{\mathrm{D}}^2(g_{\mathrm{x}}^4 - g_{\mathrm{x}}'^4)\left[p_{\mathrm{B}}q_{\mathrm{y}} + p_{\mathrm{B}}q_{\mathrm{z}} - p_{\mathrm{A}}q_{\mathrm{y}} - p_{\mathrm{A}}q_{\mathrm{z}}\right] .\end{aligned} \tag{5.40}$$

To continue, the relativistic dot products need to be expressed in terms of the Mandelstam variables for which it is necessary to look at the t-channel, u-channel and the interference terms individually.

5.4.1 *t*-channel and *u*-channel

The trace $\operatorname{Tr}\mathbb{A}_{11}$ in the invariant amplitude of the t-channel and the $\operatorname{Tr}\mathbb{A}_{22}$ in the invariant amplitude of the u-channel do not need to be calculated individually. The reason for this can be seen from Eq. 5.5: Replacing $q_1 \to q_2$ in the relativistic dot products appearing in Eq. 5.40 gives the same results with the replacement $t \to u$.
Expressing the relativistic dot products with Mandelstam variables via Eq. 5.4 and Eq. 5.5 gives

$$\begin{aligned}\operatorname{Tr}\mathbb{A}_{11} = {} & 4(g_{\mathrm{x}}^2 + g_{\mathrm{x}}'^2)^2 \left[-\frac{(t + m_{\mathrm{D}}^2 - m_\phi^2)^2}{2} - (\frac{s}{2} - m_{\mathrm{D}}^2)t + m_{\mathrm{D}}^2(\frac{s}{2} - m_{\mathrm{D}}^2 - t)\right] \\ & - 8m_{\mathrm{D}}^2(g_{\mathrm{x}}^4 - g_{\mathrm{x}}'^4)\left[t + m_{\mathrm{D}}^2 - m_\phi^2\right] - 4m_{\mathrm{D}}^4\left(g_{\mathrm{x}}^4 + g_{\mathrm{x}}'^4 - 6g_{\mathrm{x}}^2 g_{\mathrm{x}}'^2\right)\end{aligned} \tag{5.41}$$

which can be expanded to terms in powers of t and g_{x} to make the integration for the total cross section down the line simpler:

$$\begin{aligned}\operatorname{Tr}\mathbb{A}_{11} = {} & -2(g_{\mathrm{x}}^2 + g_{\mathrm{x}}'^2)^2 t^2 + 2g_{\mathrm{x}}^4\left[(2m_\phi^2 - s - 6m_{\mathrm{D}}^2)t - 9m_{\mathrm{D}}^4 - m_\phi^4 + 6m_{\mathrm{D}}^2 m_\phi^2 + m_{\mathrm{D}}^2 s\right] \\ & + 2g_{\mathrm{x}}'^4\left[(2m_\phi^2 - s + 2m_{\mathrm{D}}^2)t - m_{\mathrm{D}}^4 - m_\phi^4 - 2m_{\mathrm{D}}^2 m_\phi^2 + m_{\mathrm{D}}^2 s\right] \\ & + 4g_{\mathrm{x}}^2 g_{\mathrm{x}}'^2\left[(2m_\phi^2 - s - 2m_{\mathrm{D}}^2)t + 3m_{\mathrm{D}}^4 - m_\phi^4 + 2m_{\mathrm{D}}^2 m_\phi^2 + m_{\mathrm{D}}^2 s\right] .\end{aligned} \tag{5.42}$$

Instead of expressing t over the scattering angle ϑ in some frame of reference and integrating the differential cross section of Eq. 5.1 over the solid angle, it is easier to perform the integral over the squared matrix element with t as the integration variable.
Because of the identity Eq. 5.6 connecting t and u, choosing u as the integration variable yields the same integration interval. So the contributions of t-channel and u-channel to the total cross section are identical.

Therefore, the integral needed to calculate the contribution of both channels to the total cross section is

$$\begin{aligned} \mathbb{I}_{11} &= 4\int_{m_\mathrm{D}^2-a-b}^{m_\mathrm{D}^2-a+b} |\overline{\mathcal{M}}_1|^2 \,\mathrm{d}t = \int_{m_\mathrm{D}^2-a-b}^{m_\mathrm{D}^2-a+b} \frac{\mathbb{A}_{11}}{(t-m_\mathrm{D}^2+\hat{\imath}\varepsilon)^2}\,\mathrm{d}t \\ &\text{with } a = \frac{s}{2}-m_\phi^2,\ b = \frac{1}{2}\sqrt{(s-4m_\mathrm{D}^2)(s-4m_\phi^2)}\,. \end{aligned} \tag{5.43}$$

This expression does not diverge without the $\hat{\imath}\varepsilon$-terms as $|a| > |b|$ with

$$\begin{aligned} a^2-b^2 &= \left(m_\phi^2-\frac{s}{2}\right)^2 - \left(\frac{1}{2}\sqrt{(s-4m_\mathrm{D}^2)(s-4m_\phi^2)}\right)^2 \\ &= m_\phi^4 + \frac{s^2}{4} - m_\phi^2 s - \frac{s^2}{4} - 4m_\mathrm{D}^2 m_\phi^2 + m_\mathrm{D}^2 s + m_\phi^2 s \\ &= m_\phi^4 + m_\mathrm{D}^2(s-4m_\phi^2)\,. \end{aligned} \tag{5.44}$$

It is always $s \geq 4m_\phi^2$ as otherwise the decay is impossible by conservation of energy. Hence, the $\hat{\imath}\varepsilon$-term in the denominator of the propagators can be set to 0 moving forward as they only served to prevent a divergence.
With the anti-derivatives

$$\int \frac{1}{(t-m_\mathrm{D}^2)^2}\,\mathrm{d}t = \frac{1}{m_\mathrm{D}^2-t} \tag{5.45}$$

$$\text{and } \int \frac{1}{t-m_\mathrm{D}^2}\,\mathrm{d}t = \ln(t-m_\mathrm{D}^2)\,, \tag{5.46}$$

the indefinite integral

$$\int \frac{t}{(t-m_\mathrm{D}^2)}\,\mathrm{d}t = \ln(t-m_\mathrm{D}^2) + \frac{m_\mathrm{D}^2}{m_\mathrm{D}^2-t} \tag{5.47}$$

can be obtained by adding $\pm m_\mathrm{D}^2$ in the numerator and the anti-derivative

$$\int \frac{t^2}{(t-m_\mathrm{D}^2)}\,\mathrm{d}t = 2m_\mathrm{D}^2\ln(t-m_\mathrm{D}^2) + \frac{m_\mathrm{D}^4}{m_\mathrm{D}^2-t} + t \tag{5.48}$$

by completing the square in the numerator. Using these indefinite integrals, the definite integral $\mathbb{I}_{11}$ becomes

$$\begin{aligned} \mathbb{I}_{11} = &\left[2(g_\mathrm{x}^2+{g'_\mathrm{x}}^2)^2(2m_\phi^2-s) - 16g_\mathrm{x}^2(g_\mathrm{x}^2+{g'_\mathrm{x}}^2)m_\mathrm{D}^2\right]\ln\left(\frac{a-b}{a+b}\right) - 4(g_\mathrm{x}^2+{g'_\mathrm{x}}^2)^2 b \\ &+ \left[-2(g_\mathrm{x}^2+{g'_\mathrm{x}}^2)^2 m_\phi^4 + 16g_\mathrm{x}^2(g_\mathrm{x}^2+{g'_\mathrm{x}}^2)m_\mathrm{D}^2 m_\phi^2 - 32g_\mathrm{x}^4 m_\mathrm{D}^4\right]\frac{2b}{a^2-b^2}\,. \end{aligned} \tag{5.49}$$

5.4.2 Interference term

In case of the interference terms $\operatorname{Tr}\mathbb{A}_{12}$ and $\operatorname{Tr}\mathbb{A}_{21}$ it is again sufficient to calculate one of the two as both terms are identical. This follows from Eq. 5.40 which is unchanged when the indices x and y are switched.
Expressing Eq. 5.40 for $x = 1$ and $y = 2$ in terms of the Mandelstam variables gives

$$\begin{aligned}\operatorname{Tr}\mathbb{A}_{12} = 2(g_\mathrm{x}^2 + {g'_\mathrm{x}}^2)^2 \{&-(t + m_\mathrm{D}^2 - m_\phi^2)(u + m_\mathrm{D}^2 - m_\phi^2) \\ &-(s - 2m_\mathrm{D}^2)(m_\mathrm{D}^2 - m_\phi^2) + m_\mathrm{D}^2(s - 2m_\mathrm{D}^2 + 2m_\phi^2 - 2m_\mathrm{D}^2)\} \\ &- 4(g_\mathrm{x}^4 - {g'_\mathrm{x}}^4)m_\mathrm{D}^2(t + m_\mathrm{D}^2 - m_\phi^2 + u + m_\mathrm{D}^2 - m_\phi^2) \\ &- 4m_\mathrm{D}^4 \left(g_\mathrm{x}^4 + {g'_\mathrm{x}}^4 - 6g_\mathrm{x}^2{g'_\mathrm{x}}^2\right)\end{aligned} \tag{5.50}$$

Expanding this into terms in powers of g_x allows all but the isolated u to be eliminated due to Eq. 5.6 connecting t and u to give

$$\begin{aligned}\operatorname{Tr}\mathbb{A}_{12} = 2(g_\mathrm{x}^2 + {g'_\mathrm{x}}^2)^2 &\left(m_\mathrm{D}^2(2m_\phi^2 - s) + m_\phi^4 + m_\mathrm{D}^4 - tu\right) \\ &+ 8g_\mathrm{x}^4(s - 4m_\mathrm{D}^4) + 8g_\mathrm{x}^2{g'_\mathrm{x}}^2 s\,.\end{aligned} \tag{5.51}$$

For the integration to obtain the contribution to the total cross section the remaining u can be expressed in terms of t, again with Eq. 5.6, to give

$$\begin{aligned}\operatorname{Tr}\mathbb{A}_{12} = 2(g_\mathrm{x}^2 + {g'_\mathrm{x}}^2)^2 &\left(m_\mathrm{D}^2(2m_\phi^2 - s) + m_\phi^4 + m_\mathrm{D}^4 - t(t + s - (2m_\mathrm{D}^2 + m_\phi^2))\right) \\ &+ 8g_\mathrm{x}^4(s - 2m_\mathrm{D}^4) + 8g_\mathrm{x}^2{g'_\mathrm{x}}^2 s\,.\end{aligned} \tag{5.52}$$

The contribution to the total cross section of the interference term is proportional to the integral

$$\begin{aligned}\mathbb{I}_{12} =& 4\int_{m_\mathrm{D}^2-a-b}^{m_\mathrm{D}^2-a+b} \overline{\mathcal{M}_1\mathcal{M}_2{}^\dagger}\,\mathrm{d}t = \int_{m_\mathrm{D}^2-a-b}^{m_\mathrm{D}^2-a+b} \frac{\mathbb{A}_{12}}{(t - m_\mathrm{D}^2)(u - m_\mathrm{D}^2)}\,\mathrm{d}t \\ \text{with } a =& \frac{s}{2} - m_\phi^2,\ b = \frac{1}{2}\sqrt{(s - 4m_\mathrm{D}^2)(s - 4m_\phi^2)}\,.\end{aligned} \tag{5.53}$$

The most straightforward way to calculate this integral is starting with the anti-derivative

$$\int \frac{1}{(t - m_\mathrm{D}^2)(n - t)}\,\mathrm{d}t = \frac{\ln(t - m_\mathrm{D}^2) - \ln(t - n)}{n - m_\mathrm{D}^2} \tag{5.54}$$

which can be obtained by using partial fractions and the standard integral Eq. 5.46. From there,

$$\int \frac{t}{(t - m_\mathrm{D}^2)(n - t)}\,\mathrm{d}t = \frac{m_\mathrm{D}^2 \ln(t - m_\mathrm{D}^2) - n\ln(t - n)}{n - m_\mathrm{D}^2} \tag{5.55}$$

follows by adding $\pm m_{\mathrm{D}}^2$ to the numerator and using the same standard integral Eq. 5.46 . Finally,

$$\int \frac{t^2}{(t-m_{\mathrm{D}}^2)(n-t)}\,\mathrm{d}t = \frac{m_{\mathrm{D}}^4 \ln(t-m_{\mathrm{D}}^2) - n^2\ln(t-n)}{n-m_{\mathrm{D}}^2} - t \tag{5.56}$$

can be found by adding $\pm(n-m_{\mathrm{D}}^2)t \pm nm_{\mathrm{D}}^2)$ to the numerator, regrouping the terms and making use of both of the previous anti-derivatives.
In the concrete case of $\mathbb{I}_{12}$, there is $n = m_{\mathrm{D}}^2 - 2a$ and hence with the boundaries of Eq. 5.53 the integral becomes

$$\begin{aligned}\mathbb{I}_{12} = 4(g_{\mathrm{x}}^2 + {g'_{\mathrm{x}}}^2)^2 &\left[\frac{m_\phi^4}{a}\ln\left(\frac{a+b}{a-b}\right) - b\right] \\ &+ \frac{8}{a}\left(g_{\mathrm{x}}^4 m_{\mathrm{D}}^2(s-4m_{\mathrm{D}}^2) + g_{\mathrm{x}}^2 {g'_{\mathrm{x}}}^2 s m_{\mathrm{D}}^2\right)\ln\left(\frac{a+b}{a-b}\right).\end{aligned} \tag{5.57}$$

5.4.3 Total cross section

With the results of Eq. 5.49 for the integrated invariant amplitude of the t- and u-channel and Eq. 5.57 for the interference term, the total cross section becomes

$$\sigma_{D\bar{D}\to\phi\phi} = \frac{\alpha}{64\pi s|\vec{p}_{\mathrm{i}}|^2}\frac{\mathbb{I}_{11}+\mathbb{I}_{12}}{2} \tag{5.58}$$

due to Eq. 5.8 for the differential cross section in terms of t. Here, the factor α in front becomes relevant because the outgoing ϕ are identical particles and therefore needs to be set to $1/2$.
Hence, the final cross section of the process $D\bar{D} \to \phi\phi$ is

$$\begin{aligned}\sigma_{D\bar{D}\to\phi\phi} = \frac{1}{32\pi s(s-4m_{\mathrm{D}}^2)}\Bigg\{&\Big[(g_{\mathrm{x}}^2+{g'_{\mathrm{x}}}^2)^2(6m_\phi^4 - 4sm_\phi^2 + s^2) \\ &- 32g_{\mathrm{x}}^4 m_{\mathrm{D}}^4 + 16g_{\mathrm{x}}^2(g_{\mathrm{x}}^2+{g'_{\mathrm{x}}}^2)m_{\mathrm{D}}^2\left(s-m_\phi^2\right)\Big]\frac{1}{2a}\ln\left(\frac{a+b}{a-b}\right) \\ &+ \left[8g_{\mathrm{x}}^2(g_{\mathrm{x}}^2+{g'_{\mathrm{x}}}^2)m_{\mathrm{D}}^2 m_\phi^2 - (g_{\mathrm{x}}^2+{g'_{\mathrm{x}}}^2)^2(3m_\phi^4+2s-8m_{\mathrm{D}}^2) - 16g_{\mathrm{x}}^4 m_{\mathrm{D}}^4\right]\frac{2b}{a^2-b^2}\Bigg\}\end{aligned} \tag{5.59}$$

$$\text{with } a = \frac{s}{2} - m_\phi^2,\ b = \frac{1}{2}\sqrt{(s-4m_{\mathrm{D}}^2)(s-4m_\phi^2)} \text{ and } s \geq 4\cdot\max(m_{\mathrm{D}}^2, m_\phi^2)\,.$$

The most striking difference to the cross section of the process $D\bar{D} \to \nu\bar{\nu}$ is the presence of a logarithmic term. The condition $s \geq 4\cdot\max(m_{\mathrm{D}}^2, m_\phi^2)$ comes from conservation of energy.

The case considered in the numerical analysis is $g_\mathrm{x} = g'_\mathrm{x}$ which has the more compact cross section

$$\sigma_{D\bar{D}\to\phi\phi} = \frac{1}{8\pi s(s-4m_\mathrm{D}^2)}\Bigg[-\left(2m_\mathrm{D}^2(s-6m_\phi^2)+3m_\phi^4+4m_\mathrm{D}^4\right)\frac{2b}{a^2-b^2} + \frac{s^2+8m_\mathrm{D}^2(s-m_\phi^2)-4m_\phi^2 s+6m_\phi^4-8m_\mathrm{D}^4}{s-2m_\phi^2}\ln\left(\frac{a+b}{a-b}\right)\Bigg] \tag{5.60}$$

$$\text{with } a=\frac{s}{2}-m_\phi^2,\ b=\frac{1}{2}\sqrt{(s-4m_\mathrm{D}^2)(s-4m_\phi^2)} \text{ and } s \geq 4\cdot\max(m_\mathrm{D}^2, m_\phi^2)\,.$$

5.5 $\langle\sigma v\rangle$ at rest

For the numerical analysis of the following chapters, an approximation of $\langle\sigma v\rangle$ for low temperatures is useful. In general, such an approximation can be obtained by expanding σv in powers of v^2 around $v = 0$ which leads to an expansion of $\langle\sigma v\rangle$ in powers of $1/x$ [see 15, pp. 157]. For the purposes of this thesis, considering so called s-wave annihilation where $\langle\sigma v\rangle = \sigma v$ at $v = 0$ is sufficient.

$\langle\sigma v\rangle$ is not identical to $\langle\sigma v_\mathrm{Møl}\rangle$. It uses the relative velocity v of the annihilating particles in the lab frame where one of the particles is at rest instead of the Møller velocity $v_\mathrm{Møl}$ defined in Eq. 4.6. In the limit of $v \to 0$, both become identical and $\langle\sigma v\rangle = \langle\sigma v_\mathrm{Møl}\rangle$ [15, pp. 154]. The reason these limits are calculated for σv is that in the lab frame, there is

$$s = 2m^2\left(1+\frac{1}{\sqrt{1-v^2}}\right) \Longleftrightarrow v = \frac{\sqrt{s}\sqrt{s-4m^2}}{s-2m_\mathrm{D}^2}\,. \tag{5.61}$$

With this connection,

$$\begin{aligned}\lim_{v\to 0}\sigma_{D\bar{D}\to\nu\bar{\nu}}v &= \lim_{s\to 4m_\mathrm{D}^2}\sigma_{D\bar{D}\to\nu\bar{\nu}}\frac{\sqrt{s}\sqrt{s-4m^2}}{s-2m_\mathrm{D}^2}\\ &= \frac{3}{\pi}\frac{g_\mathrm{x}^2 g_\mathrm{n}^2 m_\mathrm{D}^2}{\left(4m_\mathrm{D}^2-m_\phi^2\right)^2+m_\phi^2\Gamma_\phi^2}\end{aligned} \tag{5.62}$$

for the annihilation cross section into two neutrinos of Eq. 5.32 follows. For the annihilation cross sections into two scalars of Eq. 5.60, the result is

$$\begin{aligned}\lim_{v\to 0}\sigma_{D\bar{D}\to\phi\phi}v &= \lim_{s\to 4m_\mathrm{D}^2}\sigma_{D\bar{D}\to\phi\phi}\frac{\sqrt{s}\sqrt{s-4m^2}}{s-2m_\mathrm{D}^2}\\ &= \frac{g_\mathrm{x}^4 m_\mathrm{D}\sqrt{m_\mathrm{D}^2-m_\phi^2}}{2\pi\left(2m_\mathrm{D}^2-m_\phi^2\right)^2}\end{aligned} \tag{5.63}$$

for $m_{\mathrm{D}} \geq m_\phi$ since the limit of the logarithmic term is

$$\lim_{s \to 4m_{\mathrm{D}}^2} \sqrt{s - 4m_{\mathrm{D}}^2}^{-1} \ln\left(\frac{a+b}{a-b}\right) = \frac{2\sqrt{m_{\mathrm{D}}^2 - m_\phi^2}}{2m_{\mathrm{D}}^2 - m_\phi^2}\,. \tag{5.64}$$

For $m_{\mathrm{D}} < m_\phi$, the annihilation is not possible for $v = 0$ as $s < 4m_\phi^2$ would violate conservation of energy and so $\lim_{v \to 0} \sigma_{D\bar{D} \to \phi\phi} v = 0$.

6 Numerical Solution of the Boltzmann Equation

In this chapter, the analytical cross sections obtained in the previous chapter are used to constrain the possible values of the masses m_{D} and m_ϕ as well as the couplings g_{x} and g_{n} by numerically solving the differential equation Eq. 4.12 and comparing the resulting yield to the observed relic density of $\Omega_{\mathrm{c}}h^2 = 0.120 \pm 0.001$. This significantly restricts the viable parameter space of the model.
The simulation is implemented in `MATLAB` [19] and compared to results obtained from `micrOMEGAs` [20].

6.1 Implementation in `MATLAB`

`MATLAB` provides multiple solvers for Ordinary Differential Equations (ODE) and therefore makes the numerical simulation relatively straightforward. These solvers automatically adjust the step width according to the stiffness of the equation and also allow the user to specify the desired errors. These features are crucial for the ODE at hand because the resulting function $Y(x)$ follows the exponentially decreasing equilibrium yield Y_{eq} for $x \lesssim 1$ and then decouples from it to become constant for $x \gtrsim 50$. Hence, small x require small step widths of 10^{-5} and below, while for large x even steps of $\mathcal{O}(1)$ can be taken without sacrificing accuracy.
The chosen solver is called `ode15s`, uses the variable order method and is the most precise solver for stiff problems [21]. The line of code

```
1 [x,Y] = ode15s(@(x,Y) BoltzmannEquation(x,Y,massDCurrent,massPhiCurrent,...
2         gXCurrent,gNuCurrent,constWithSqrtG,gInternal,decayWidthOfPhi,...
3         gstar_tmp,heff_tmp), criticalInterval, initialCondition, options);
```

uses it to extrapolate the Boltzmann equation 4.12 for the Yield Y in terms of x over the interval specified in `criticalInterval` and stores the evaluated points for x and Y as column vectors in the variables of the same name. The 1×2 matrix `criticalInterval` has the starting point x_{s} as the first and the end point x_{e} as the second element. The starting point for the broader scans of Section 6.4 onward is $x_{\mathrm{s}} = 1$, the sections before use $x_{\mathrm{s}} = 0.3$) and $x_{\mathrm{e}} = 350$ as the end point.
The argument `initialCondition` contains the yield $Y_0 \equiv Y(x_{\mathrm{s}})$. At $x \lesssim 1$ the thermally averaged cross section will be so large that $Y(x) = Y_{\mathrm{eq}}(x)$ and so the initial condition is

$Y_0 = Y_{\mathrm{eq}}(x_{\mathrm{s}})$ This holds for all parameters investigated in this thesis. However, for small enough couplings the freeze-out happens even before this point.

The argument `options` contains a number of optional parameters for the solver. Most importantly, these are relative and absolute error tolerances. The absolute error tolerance is set to be ignored because of the exponentially decreasing yield.

Finally, the function `BoltzmannEquation` implements the right hand side of Eq. 4.12 with the $\langle \sigma v_{\mathrm{Møl}} \rangle$ as Eq. 4.26 where the total cross section is $\sigma = \sigma_{D\bar{D}\to\phi\phi} + \sigma_{D\bar{D}\to\nu\bar{\nu}}$. It takes the four parameters of the model as arguments as well as constants which do not need to be calculated in every step of the iteration. Moreover, the interpolants `gstar_tmp` and `heff_tmp` for the effective degrees of freedom are passed as arguments to this function so that they do not have to redefined every time `BoltzmannEquation` is called.

Using `ode15s` to continue the solution until today's photon temperature T_0 is inefficient because for the relevant masses in the GeV to TeV range, $T_0 = (2.725\,28 \pm 0.000\,57)\,\mathrm{K}$ [22] (corresponding to $T_0 = (234.891 \pm 0.049)\,\mu\mathrm{eV}$ in natural units) is reached when x is at least of order 10^{13}. The more efficient solution is to drop Y_{eq} from the differential equation Eq. 4.1 at some temperature T_{d} after freeze-out where $Y \gg Y_{\mathrm{eq}}$. This differential equation has the integral solution

$$\frac{1}{Y(T_0)} = \frac{1}{Y(T_{\mathrm{d}})} + \sqrt{\frac{\pi}{45G}} \int_{T_0}^{T_{\mathrm{d}}} \sqrt{g_*} \langle \sigma v_{\mathrm{Møl}} \rangle \, \mathrm{d}T \,. \tag{6.1}$$

After $x \approx 350$ the Bessel functions in the formulas cause underflow errors. Therefore, the above equation is used after $T_{\mathrm{d}} = m_{\mathrm{D}}/350$ and $\langle \sigma v_{\mathrm{Møl}} \rangle$ is replaced by the σv at $v = 0$ from Section 5.5.

The formula for the relic density today is

$$\Omega_{\mathrm{c}} h^2 = \frac{\rho_{\mathrm{c}}}{\rho_{\mathrm{crit}}} h^2 = 2 \frac{m_{\mathrm{D}} Y(T_0) s(T_0)}{3/\left(8\pi G\right)} \left(100 \, \frac{\mathrm{Mpc}}{\mathrm{km} \cdot \mathrm{s}} \right)^{-2} = 2 \cdot 1.3775 \cdot 10^7 Y(T_0) \frac{m_{\mathrm{D}}}{\mathrm{GeV}} \frac{T_0^3}{\mathrm{K}^3} \tag{6.2}$$

because $h_{\mathrm{eff}}(T_0) = 3.9387$ [13]. The factor of 2 accounts for D and $\bar{D}$.

6.2 Evolution of the yield with temperature

Before delving into broader scans of the parameter space focused on $\Omega_{\mathrm{c}} h^2$, it is useful to look at the raw output of ode15s to check whether the resulting curves for the yield match the expected shape shown in Fig. 4.1. As a representative example, Fig. 6.1 shows Y as a function of x for different couplings g_{x} with all other parameters staying identical. The resulting curves match the expectations perfectly: For $x \lesssim 10$ the yield follows the equilibrium distribution and then decouples to become essentially constant for $x \gtrsim 200$. This happens later for higher g_{x} and thus higher cross sections which leads to a lower final yield.

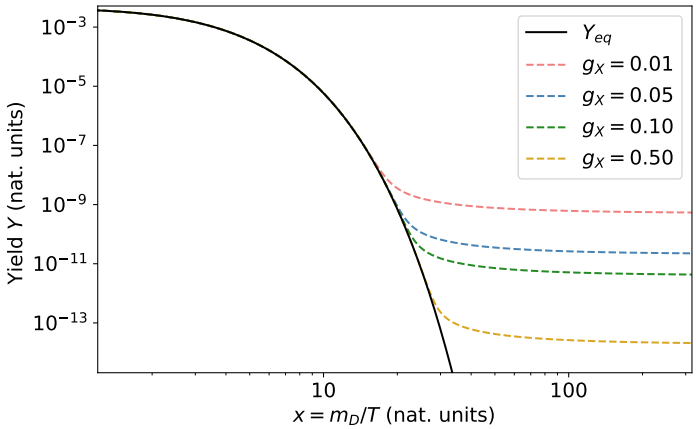

Figure 6.1: Yield Y as a function of x with $m_{\mathrm{D}} = 50\,\mathrm{GeV}$, $m_\phi = 5\,\mathrm{GeV}$ and $g_{\mathrm{n}} = 0.1$ compared to the equilibrium distribution Y_{eq}.

Another interesting parameter to look at is the ratio between the masses of the scalar and the fermion $R = m_\phi/m_{\mathrm{D}}$. For ratios below $R \lesssim 1/5$, this has almost no impact on the cross section because all terms containing m_ϕ are in even powers and therefore suppressed by at least a factor of $1/25$. For higher R, there are two competing effects from the two annihilation channels.

The cross section $\sigma_{D\bar{D}\to\nu\bar{\nu}}$ monotonously increases with R in the region of the parameter space with $R < 2$ which this thesis investigates. Hence, the final yield should become lower for increasing R if this process is dominant. However, since the cross section $\sigma_{D\bar{D}\to\phi\phi}$ monotonously decreases with R, these effects almost cancel out for $R \lesssim 1.2$ if the couplings g_{x} and g_{n} are identical. This can be seen in Fig. 6.2. For higher R, the process $D\bar{D} \to \phi\phi$ becomes kinematically inaccessible - since it requires the fermions to have a significant amount of kinetic energy if they are lighter than the scalars - so early on that the process $D\bar{D} \to \nu\bar{\nu}$ is most relevant and the final yield decreases. These properties of the cross sections are dealt with in more detail in the following Section 6.3.

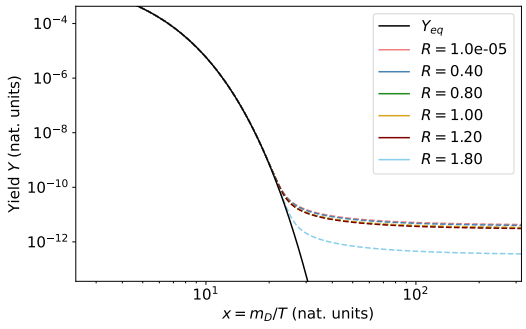

Figure 6.2: Yield Y as a function of x with $m_{\mathrm{D}} = 50\,\mathrm{GeV}$ and $g_{\mathrm{x}} = g_{\mathrm{n}} = 0.1$ compared to the equilibrium distribution Y_{eq}.

Fig. 6.3 shows the freeze-out for different R when $\langle\sigma v_{\mathrm{Møl}}\rangle$ is dominated by one of the two processes because of a disparity between the couplings and thus isolates the behavior of the cross sections discussed above. So while the final yield decreases with R in Fig. 6.3a where the process $D\bar{D} \to \nu\bar{\nu}$ is stronger by a factor of ~ 100 because of the couplings, the same

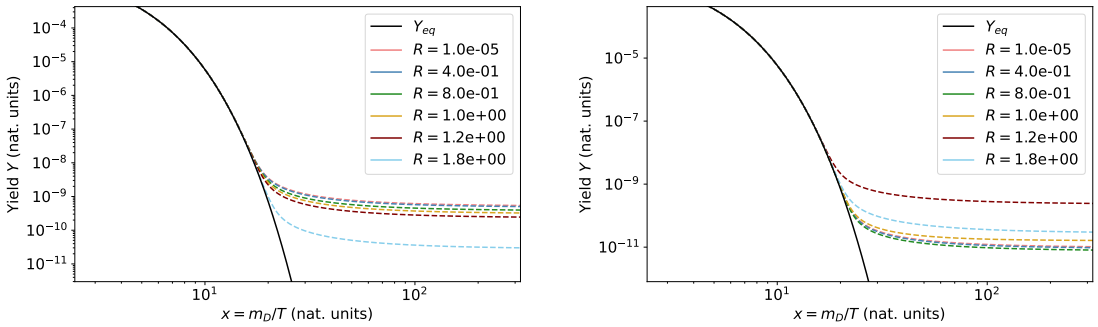

(a) (b)

Figure 6.3: Yield Y as a function of x with $m_{\mathrm{D}} = 50\,\mathrm{GeV}$. The figure on the left shows curves where $g_{\mathrm{x}} = 0.01$ and $g_{\mathrm{n}} = 0.1$ and therefore the annihilation into neutrinos is dominant. Here, the final yield increases with the mass ratio $R = m_\phi/m_{\mathrm{D}}$. In the figure on the right, there is $g_{\mathrm{x}} = 0.1$ and $g_{\mathrm{n}} = 0.01$, and hence the annihilation into scalars is the primary process. For $R > 1$, the decay into neutrinos becomes increasingly important.

cannot be said for the opposite case shown in Fig. 6.3b. Here, the final yield increases with R but then drops off again when R becomes significantly larger than 1. This is again because $D\bar{D} \to \phi\phi$ becomes kinematically inaccessible for low temperatures and so the annihilation into neutrinos is dominant regardless of the choice of couplings.

An important observation to make is that $\langle\sigma v_{\mathrm{Møl}}\rangle$ decreases quadratically when the absolute mass scale is increased, i.e. higher m_{D} but R stays constant. This follows from the substitution $\tilde{s} = s/m_{\mathrm{D}}^2$ in $\langle\sigma v_{\mathrm{Møl}}\rangle$ (see Eq. 4.26) and the fact that σ has units of GeV^{-2}. The right hand side of the differential equation Eq. 4.1 contains an additional factor m_{D} as well as the degrees of freedom g_*. The latter only varies about a factor of 10 from the early universe until today. Hence, an increase in the mass scale makes the right hand side of Eq. 4.1 smaller and amounts to a higher final yield. This can be seen in Fig. 6.4.

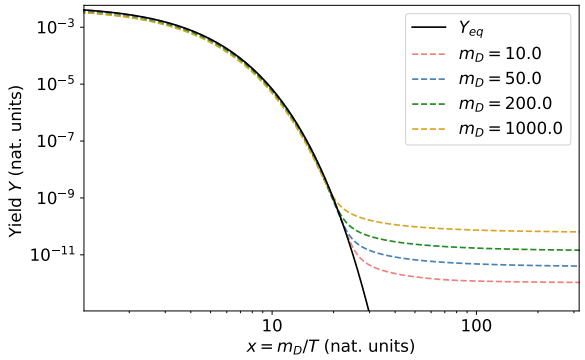

Figure 6.4: Yield Y as a function of x with for different m_{D} in units of GeV. The other input parameters are $g_{\mathrm{x}} = g_{\mathrm{n}} = 0.1$ and $R = 0.4$. As argued above, the yield increases with m_{D}. Y_{eq} shown in the plot is for $m_{\mathrm{D}} = 10\,\mathrm{GeV}$.

The reason the yields are not quite identical for small x in this figure lies in the fact that the equilibrium distribution depends not only on x but also the absolute temperature through the degrees of freedom $h_{\text{eff}}(T)$. Y_{eq} shown in the plot is for $m_{\text{D}} = 10\,\text{GeV}$.

6.3 Interaction rates and $\langle \sigma v_{\text{Møl}} \rangle$

The previous section alluded to the behavior of the two different cross sections included in $\langle \sigma v_{\text{Møl}} \rangle$. Fig. 6.5a shows $\langle \sigma v_{\text{Møl}} \rangle$ with just $\sigma_{D\bar{D}\to\nu\bar{\nu}}$ and $\sigma_{D\bar{D}\to\phi\phi}$ for different values of R. While $\sigma_{D\bar{D}\to\nu\bar{\nu}}$ increases with R, $\sigma_{D\bar{D}\to\phi\phi}$ decreases and does not stay finite for $R > 1$ but instead rapidly decreases with temperature T because the DM particles rarely have enough energy for $T \ll m$ to enable an annihilation into two scalars. In any case, for $g_{\text{x}} = g_{\text{n}}$ like in Fig. 6.5a $D\bar{D} \to \nu\bar{\nu}$ is always the dominant process.

An important aspect visible in Fig. 6.5a is that if $\langle \sigma v_{\text{Møl}} \rangle$ stays finite for a process, it asymptotically approaches a maximum value. Since both cross sections scale $\propto 1/s$ - disregarding mass terms - and their values at higher s are exponentially suppressed in the thermal average (see Eq. 4.26), this value is just $\langle \sigma v_{\text{Møl}} \rangle$ at $T = 0$ which is $\sigma v_{\text{Møl}}$ at $s = 4m_{\text{D}}^2$. This property is useful in the following Chapter 7.

The same dependency of $\langle \sigma v_{\text{Møl}} \rangle$ on T also translates into the interaction rates $\Gamma = n\langle \sigma v_{\text{Møl}} \rangle$. As explained in the beginning of Chapter 4, these should only drop below the Hubble parameter H when n decouples from the equilibrium distribution. Fig. 6.5b shows that this is indeed the case. However, if the couplings are decreased by more than approximately two orders of magnitude, then the interaction rate is lower than the H for all values of x shown here. In this case, freeze-out happens for $x \ll 1$ if at all and the approach of Chapter 4 fails. Fortunately, such couplings produce a relic density orders of magnitude above the observed values and so this case is generally not relevant.

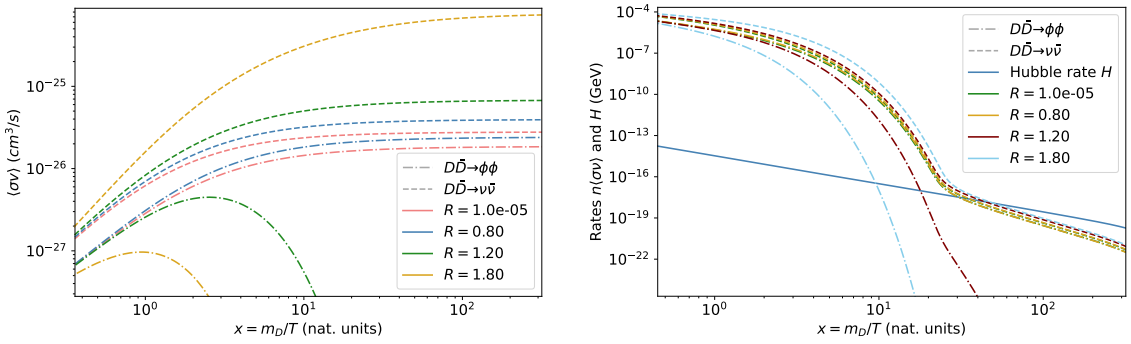

(a) (b)

Figure 6.5: (a) $\langle \sigma v_{\text{Møl}} \rangle$ for both relevant annihilation processes with $g_{\text{n}} = g_{\text{x}} = 0.1$ and $m_{\text{D}} = 50\,\text{GeV}$ as a function of x. (b) The interaction rates $n\langle \sigma v_{\text{Møl}} \rangle$ compared to the Hubble parameter H for $m_{\text{D}} = 50\,\text{GeV}$ and $g_{\text{x}} = g_{\text{n}} = 0.1$

6.4 Restriction through the final relic density

Without further ado, Fig. 6.6 shows one scan of the parameter space for constant couplings $g_\mathrm{x} = g_\mathrm{n} = 0.1$ as a heat map, in which relic densities with $0.11 < \Omega_\mathrm{c}h^2 < 0.13$ are highlighted in green. For $R \lesssim 0.25$, this parameter has negligible impact on the final relic density and the necessary dark matter mass m_D is around 50 GeV. Until the mass of the scalar reaches the dark matter mass at $R = 1$, the necessary dark matter mass increases slightly due to the fact that the cross section for the annihilation into neutrinos increases slightly faster than the cross section for the annihilation into scalars decreases. This changes at $R = 1$ when the process $D\bar{D} \to \phi\phi$ is no longer possible at rest, i.e. the thermally averaged cross section times velocity for this processes rapidly decreases for temperatures $T \ll m_\mathrm{D}$. Past this point, the required m_D increases rapidly with R, reaching $m_\mathrm{D} \approx 550\,\mathrm{GeV}$ for $R = 1.9$ because $\sigma_{D\bar{D}\to\nu\bar{\nu}}$ increases rapidly in this regime as the resonance occurs at $s = m_\phi^2$ which can be met for $R \geq 2$.

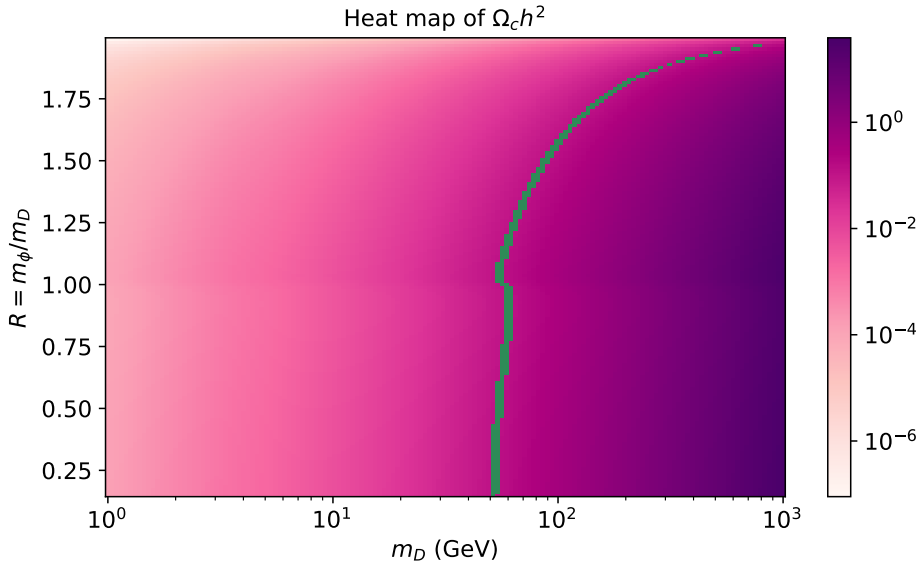

Figure 6.6: A logarithmically scaled heat map showing the relic density $\Omega_\mathrm{c}h^2$ for $g_\mathrm{x} = g_\mathrm{n} = 0.1$ obtained from the `MATLAB` simulation. The green region marks where $0.11 < \Omega_\mathrm{c}h^2 < 0.13$ is fulfilled.

The qualitative behavior of the relic density $\Omega_\mathrm{c}h^2$ stays the same for all couplings but shifts in the mass axis as is to be expected from the behavior of the yield discussed in the previous section: Higher couplings decrease the final yield for identical masses and so the mass required to meet the observed relic density increases. If the coupling g_n becomes stronger relative to g_x the shift at $R = 1$ disappears because the annihilation into scalars is then always negligible and conversely if g_x is the stronger coupling the shift becomes more pronounced.

As a result, Eq. 3.15 limiting the decay width of ϕ to less than 1 s is almost irrelevant. It

only excludes extremely small values of both g_{n} or m_ϕ.

6.5 Comparison to the results from `micrOMEGAs`

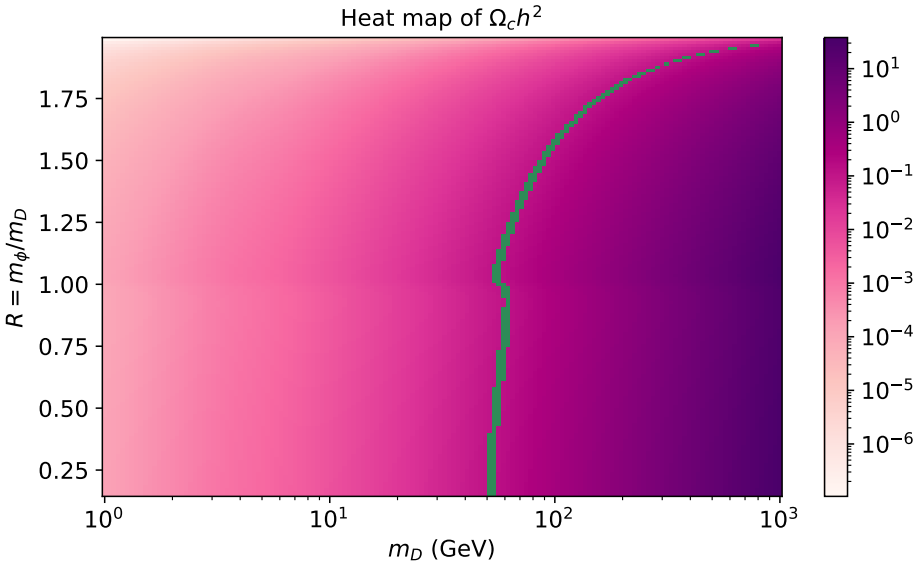

Figure 6.7: A logarithmically scaled heat map showing the relic density $\Omega_{\mathrm{c}} h^2$ for $g_{\mathrm{x}} = g_{\mathrm{n}} = 0.1$ obtained from `micrOMEGAs`. The green region marks where $0.11 < \Omega_{\mathrm{c}} h^2 < 0.13$ is fulfilled.

`micrOMEGAs` is a well established software which numerically solves the Boltzmann equation as well as determines exclusion limits from direct as well as indirect detection from a variety of sources. The code as well as the documentation can be found here [20]. It requires the dark matter model to be specified in .mdl-files. For the Lagrangian of this thesis, this task has kindly been performed by Dr. Amin Abou Ibrahim.

Unfortunately, the possibilities of `micrOMEGAs` with respect to dark matter detection are mostly not applicable to the model investigated here as it only couples to neutrinos. There is a possibility to compare the generated neutrino flux with results of IceCube22 to check whether these are sufficient to exclude the model indirectly but the method used in the following chapter allows to include more neutrino detection experiments for the indirect exclusion limits thanks to the work done in [23]. Therefore, the only functionality used here is the solution of the Boltzmann equation to obtain the resulting relic density.

Fig. 6.7 shows the results from `microOMEGAs_5.3.41` for the same parameters as Fig. 6.6. The `python` script used to loop over different model parameters has been provided by Dr. Amin Abou Ibrahim.

The qualitative behavior is identical to the results from `MATLAB` presented in the previous sections. However, looking at the relative difference between the calculated relic densities from `MATLAB` and `micrOMEGAs` plotted in Fig. 6.8 shows that there is a systematic discrepancy between the two simulations although the results from `MATLAB` and `micrOMEGAs` generally differ by less than 5 %.

The differences are partially due to the s-wave approximation after $x = 350$ which overestimates $\langle \sigma v_{\text{Møl}} \rangle$. The impact of this shortcoming is especially pronounced for high R due to the resonance of $\sigma_{D\bar{D}\to\nu\bar{\nu}}$ as well as low masses m_{D} since σ increases quadratically when m_{D} is decreased and R is kept constant (this is discussed at the end of Section 4.2 as well). Both combine to cause a relative difference of as low as $-15\,\%$ for $R \to 2$ and $m_{\text{D}} = 1\,\text{GeV}$.

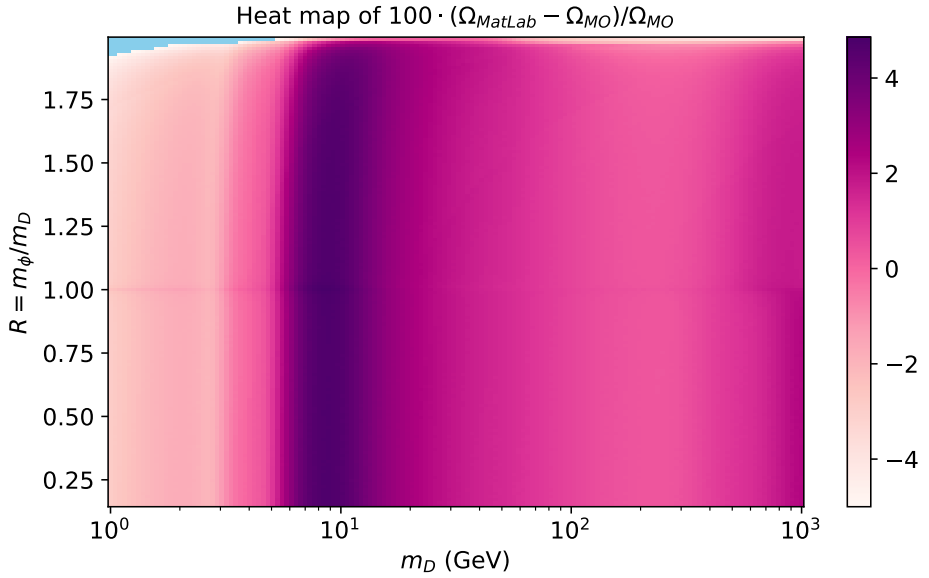

Figure 6.8: A heat map showing of the relative deviations between the results of `micrOMEGAs` and `MATLAB`. The results generally deviate by less than 5 %. However, for large R and small m_{D} the difference increases due to the resonance in $\sigma_{D\bar{D}\to\nu\bar{\nu}}$. The blue region shows where the relative difference is less than -5 % as otherwise the other features become indistinguishable.

Apart from this region, the difference is especially pronounced for masses around 7 GeV regardless of the other parameters which indicates that the another source for the differences might lie with the degrees of freedom g_*. These have a sharp drop around 150 MeV because of the QCD phase transition. The precise shape of this drop is the biggest difference between different approaches to calculating the degrees of freedom. For masses of a few GeV, this drop occurs right after decoupling and therefore has a significant impact on the relic density. This is what Drees et al. found in their paper as well from which the degrees of freedom used in the `MATLAB` code are taken from [13].

This paper compared multiple sets of the degrees of freedom for generic forms of $\langle \sigma v_{\text{Møl}} \rangle$, namely proportional to $1/x$ and a constant $\langle \sigma v_{\text{Møl}} \rangle$ chosen so that $\Omega_{\text{c}} h^2 = 0.1193$. Fig. 6.9a

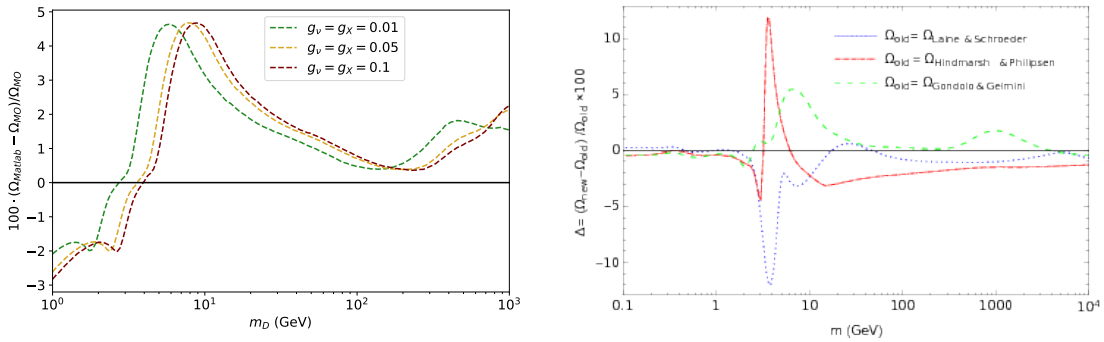

(a) (b)

Figure 6.9: (a) The relative difference between the results from `MATLAB` and `micrOMEGAs` for different couplings at $R = 0.5$. (b) For comparison, this plot from [13] shows the impact of different sets for the degrees of freedom on pure p-wave annihilation with $\langle \sigma v_{\text{Møl}} \rangle = x^{-1} \cdot 1.2 \cdot 10^{-24}\,\text{cm}^3/\text{s}$. The simulation in `MATLAB` uses the degrees of freedom from [13] and `micrOMEGAs` those labeled 'Gondolo & Gelmini' [24]. Fig. 6.9a reproduces many of the features seen in Fig. 6.9b but in addition there are systematic discrepancies because of the s-wave approximation.

compares the relative difference between the `MATLAB` and `micrOMEGAs` simulation for different couplings and Fig. 6.9b shows the results of [13] for a generic $\langle \sigma v_{\text{Møl}} \rangle$ of $x^{-1} \cdot 1.2 \cdot 10^{-24}\,\text{cm}^3/\text{s}$. The bright green curve marked as 'Gondolo & Gelmini' is what one would roughly expect to be the result from comparing the simulation in `MATLAB` to `micrOMEGAs` since the paper by Gondolo and Gelmini [15] uses the same source for their degrees of freedom h_{eff} and g_{eff} as `micrOMEGAs` (see [15, p. 159] and [24, p. 8]): two papers from Olive et al. from 1981 [25] and 1988 [26].

And indeed, the same patterns found in [13] show up in Fig. 6.9a, especially the peak in the relative deviations at masses of a few GeV. Its position shifts towards smaller masses for lower couplings since then the decoupling happens slightly earlier but the general shape stays. Furthermore, the relative differences for the smallest couplings $g_{\text{x}} = g_{\text{n}} = 0.01$ shown in Fig. 6.9a have another peak at $m_{\text{D}} \approx 450\,\text{GeV}$ which is what can be seen in Fig. 6.9b for masses around 1 TeV as well. For higher couplings, this peak occurs after 1 TeV and is therefore not visible in Fig. 6.9a.

The reason that the relative difference becomes negative for masses of $\lesssim 3\,\text{GeV}$ is that $\langle \sigma v_{\text{Møl}} \rangle$ increases when m_{D} is decreased and so the s-wave approximation is worse. This leads to a too low relic density.

There are two more differences which in principle contribute to the systematic differences but have completely negligible impact. The first is that `micrOMEGAs` uses $1.1 \cdot Y_{\text{eq}}$ as the initial condition [20] whereas the `MATLAB` code uses just Y_{eq}. Since before decoupling, Y tends toward Y_{eq}, the influence on the results of such a small difference is irrelevant.

The second is the approximate solution Eq. 6.1 which `micrOMEGAs` uses after $Y \geq 10 Y_{\text{eq}}$ [20] whereas the `MATLAB` code uses it for $x \geq 350$. For both cases, the influence of Y_{eq} is always

negligible.

Another improvement would be to include the particles of the hidden sector in the effective degrees of freedom $g_{\text{eff}}(T)$ and $h_{\text{eff}}(T)$ since they also contribute to the total energy and entropy densities. Freeze-out happens for $m_{\text{D}} > T$ where their contribution is already exponentially suppressed (see Eq. 3.10) and Eq. 6.2 for the final relic density only explicitly depends on the entropy density which the frozen-out particles do not contribute to. So would not change the relic density by much and is also not implemented in `micrOMEGAs`.

6.6 Using bisection to restrict the parameter space

All analysis up to now was done by looping over different values for the model parameters. This works well enough but is rather inefficient since the scan Fig. 6.6 shows that even the restriction $\Omega_{\text{c}}h^2 = 0.120 \pm 0.010$, a tolerance of 10 times larger than the uncertainty of the experimental value [1], excludes the vast majority of the parameter space. Therefore, if a more detailed restriction of the viable parameter space is desired simply looping will evaluate a lot of points whose relic density is off by orders of magnitude.

A better option is to use the observation from Section 6.2 that $\Omega_{\text{c}}h^2$ monotonously decreases with g_{x} and monotonously increases with m_{D} if R, g_{n} and the respective other parameter are kept constant [5].

This means that bisection can be used to find the parameters producing the desired relic density more efficiently. The code in Appendix C implements this with the bisection being done for the parameter g_{x} while all other parameters are still simply looped over. The code could easily be changed to a bisection in m_{D} if desired. In this case, the initial condition has to be reset for each step.

Fig. 6.10 illustrates the procedure of the bisection code. It starts by solving the Boltzmann equation for one coupling which produces a too high relic density and one which produces a too low relic density. Both of these have to be set manually. For the model at hand, $g_{\text{x}} = 10^{-4}$ produces a too high relic density for almost all investigated masses. While Section 6.3 shows that this coupling is so low that the freeze-out happens before the simulated interval of x for some masses, this does not impact the functionality of the code as then the relic density is above the observed values by orders of magnitude. The simulations give the same result and even though the precise value might be far off, this is of no consequence for a bisection algorithm.

A sensible choice for a coupling producing too low a relic density is $g_{\text{x}} = \sqrt{4\pi}$. This is because for higher couplings, the matrix element for the self-scattering process $D\bar{D} \to D\bar{D}$ will always

[5] The relic density will also be monotonous in g_{n} for the most part. However, at the resonance $s = m_\phi$ of $\sigma_{D\bar{D}\to\nu\bar{\nu}} \propto g_{\text{n}}^{-2}$ and so there will be issues for some parts of the parameter space.

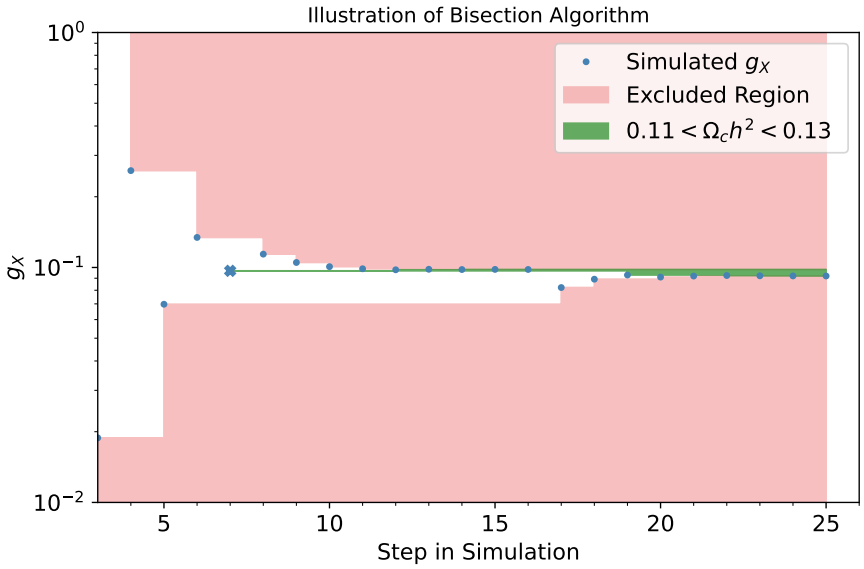

Figure 6.10: An example of the procedure implemented in the simulation code in Appendix C: The blue points represent the simulated g_x, which up to the x-shaped marker are the geometric mean of current upper and lower bound on g_x and exclude values for g_x, which do not produce the desired relic density. The excluded values are shaded red. In this figure, the desired relic density is set to $0.11 < \Omega_\mathrm{c}h^2 < 0.13$. The x-shaped marker shows, where the relic density is first in this interval. After that, bisection is used to approximate $\Omega_\mathrm{c}h^2 = 0.11$ and then $\Omega_\mathrm{c}h^2 = 0.13$, which widens the green shaded region, which shows where $0.11 < \Omega_\mathrm{c}h^2 < 0.13$ is met.

exceed unity when integrated over the angle of both outgoing particles and only the simplest diagram (Fig. 5.3 with the neutrinos replaced by D and $\bar{D}$) is considered.

After these initial values, the code solves the Boltzmann equation for the coupling that is the geometric mean of the highest coupling producing a relic density over a specified threshold and the lowest coupling producing a relic density under another specified threshold. The geometric mean is the better choice compared to the usual arithmetic mean since the coupling has a roughly exponential effect on the relic density and the geometric mean takes the arithmetic mean of the logarithms:

$$\sqrt{ab} = \sqrt{\exp\left(\ln a + \ln b\right)} = \exp\left(\frac{\ln a + \ln b}{2}\right) \tag{6.3}$$

The function `CloseInBoundaries` then checks whether the relic density is too high, too low or fits within the desired interval set in the file `Parameters.m` as `densityBoundaries`. As long as it does not fit, bisection continues up to a maximum number of steps and in this way excludes an increasing amount of the parameter space. In Fig. 6.10, this is shaded red. The current parameters closest to producing the desired relic density are stored in `currentBounds`. If the relic density is within the desired interval, which in Fig. 6.10 first happens after 7 iterations, the code proceeds to bisect on the edges of the region which produces the correct relic density

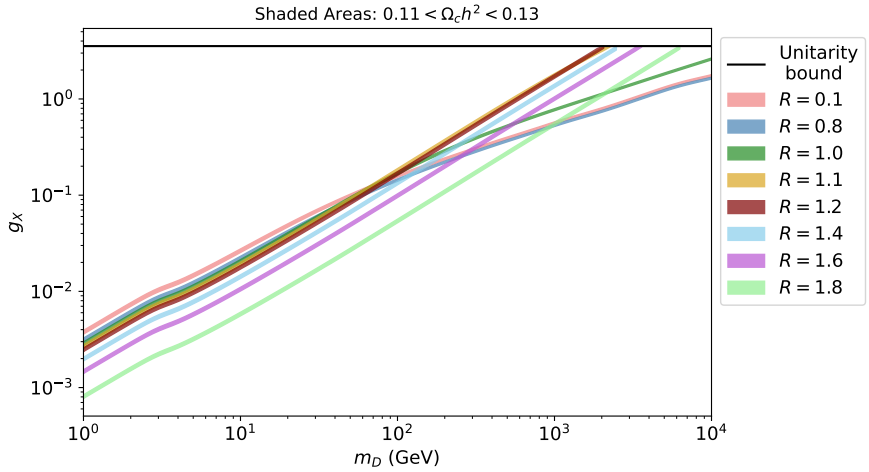

Figure 6.11: The shaded areas show the region where the condition $0.11 < \Omega_c h^2 < 0.13$ is met. The coupling g_n is set to 0.1 in this plot.

through the function `FindNewBoundaries`. This way, the region which is known to give the desired relic density, shaded green in Fig. 6.10, and the region which is known to not give the desired relic density come increasingly closer together.

In Fig. 6.11, the resulting regions with the desired relic density are plotted as a function of m_D. As is to be expected, the required g_x increases monotonously with m_D and decreases with R for $R \gtrsim 1$. For $R < 1$ and $m_D \gtrsim 500\,\text{GeV}$, the required g_x exceeds 0.1 and as the plot uses $g_n = 0.1$, this means that here $D\bar{D} \to \phi\phi$ takes over and the total $\langle \sigma v_{\text{Møl}} \rangle$ now scales quartically instead of quadratically with g_x. As a result, the required g_x increases more slowly with m_D. Additionally, the width of the interval in g_x fulfilling $0.11 < \Omega_c h^2 < 0.13$ appears to increase exponentially with m_D.

7 Restrictions from the Measured Neutrino Flux

Since the DM of this model couples to neutrinos, annihilations produce a flux of neutrinos which can be measured and turned into limits on the model parameters. This has been done independent of the specific model in [23] by Argüelles et al. for a variety of neutrino detection experiments.

The results of their calculations for s-wave annihilations into two neutrinos are shown in Fig. 7.1. Since the expected flux is proportional to the thermally averaged self annihilation cross section times velocity into all neutrino flavors $\langle \sigma v \rangle$, the measured flux gives upper limits on the size of this cross section independent of the specific model which currently exclude the shaded regions in Fig. 7.1. The dashed lines show the expected results from future experiments.

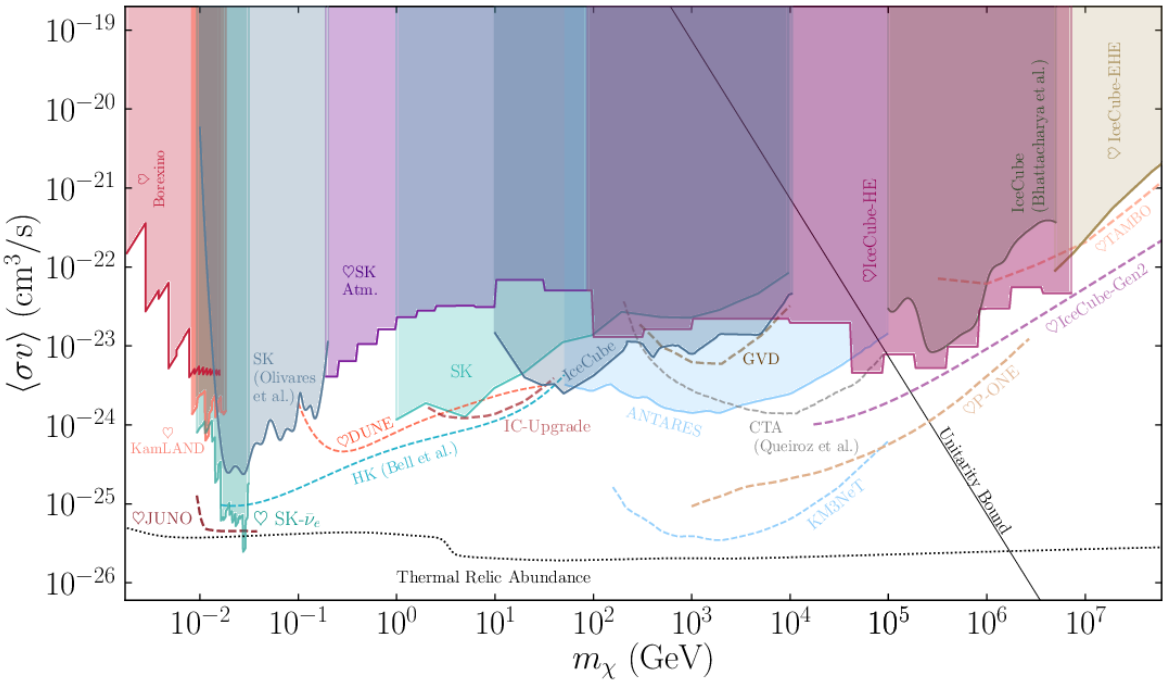

Figure 7.1: Fig. 2 of [23]: It illustrates the excluded regions for $\langle \sigma v \rangle$ into all neutrino flavors in the case of s-wave annihilation through the measured neutrino flux (solid lines/ shaded regions) and projected measurements (dashed lines). The black dotted line shows the required $\langle \sigma v \rangle$ to produce the observed relic abundance, if $\langle \sigma v \rangle$ is constant. The limits shown are for single particle Majorana DM and need to be multiplied by a factor of 2 for single particle Dirac DM like the model of this thesis.

The limits of Fig. 7.1 are for a Majorana DM particle and need to be multiplied by a factor of 2 for Dirac DM which is the case of this model. Additionally, the limits in Fig. 7.1 hold only for s-wave annihilation, that is when $\langle\sigma v\rangle$ can be approximated as σv at $v = 0$. In principle, $\langle\sigma v\rangle$ at small temperatures $T \ll m_\mathrm{D}$ can be obtained by expanding σv in powers of v^2 which leads to an expression for $\langle\sigma v\rangle$ in powers of T [see 15, pp. 157]. There are models, where most annihilations even at today's temperature of $T_0 = (234.891 \pm 0.049)\,\mu\mathrm{eV}$ [22] do not happen at $v = 0$ and hence [23] also calculates limits for the higher order $p-$ and $d-$wave annihilations ($\propto v^2$ and $\propto v^4$, respectively) but these are a lot weaker and not relevant to the model of this thesis. The s-wave approximation of $\langle\sigma v\rangle$ for this model can be found in Section 5.5.

The calculations of [23] only take into account annihilations into two neutrinos. For the model of this thesis, the scalar portal ϕ also decays into neutrinos and as the annihilations happen at rest this means that the process $D\bar{D} \to \phi\phi$ is only possible for $m_\mathrm{D} \geq m_\phi$. With this condition, ϕ always decays into two neutrinos and so $D\bar{D} \to \phi\phi$ effectively produces four neutrinos, each with an energy of $m_\mathrm{D}/2$. Since the limits of Fig. 7.1 are not strongly dependent on the neutrino energy, the total cross section on which the limits of Fig. 7.1 are imposed can be approximated by

$$\langle\sigma v\rangle = \langle\sigma_{D\bar{D}\to\nu\bar{\nu}} v\rangle + 2\langle\sigma_{D\bar{D}\to\phi\phi} v\rangle \tag{7.1}$$

for $v = 0$. The correct treatment of decays into four neutrinos would require the limits of Fig. 7.1 to be recalculated which is a task out of the scope of this thesis.

The cross sections were calculated in Section 5.5 and are now used to turn the limits shown in Fig. 7.1 into limits on the parameter space of the model of this thesis. The relevant data sets have been provided by the authors of [23] on request of Dr. Amin Abou Ibrahim and the projected limits on KM3NeT have been extracted from the plot using `WebPlotDigitizer` [27].

7.1 Limits on the parameter space

Today, indirect detection via the neutrino flux imposes no additional constraint to the observed relic density which agrees with the findings of [23]. Fig. 7.2 shows the regions excluded through the neutrino flux for $g_\mathrm{x} = g_\mathrm{n}$, both from existing detection data and projected experiments, as well as the parameters, for which the relic density from the simulation with `MATLAB` fulfills $0.11 < \Omega_\mathrm{c} h^2 < 0.13$.

In the mass range around 10 GeV where the limits of Fig. 7.2 occur, these are set by the data from Super-Kamiokande (SK) and the projected sensitivity of Hyper-Kamiokande (HK). For larger couplings than $g_\mathrm{x} = g_\mathrm{n} = 0.1$ which are used for Fig. 7.2, the projected sensitivity of

KM3NeT comes into play but is also not sufficient to exclude any portion of the parameter space which leads to the observed relic density.

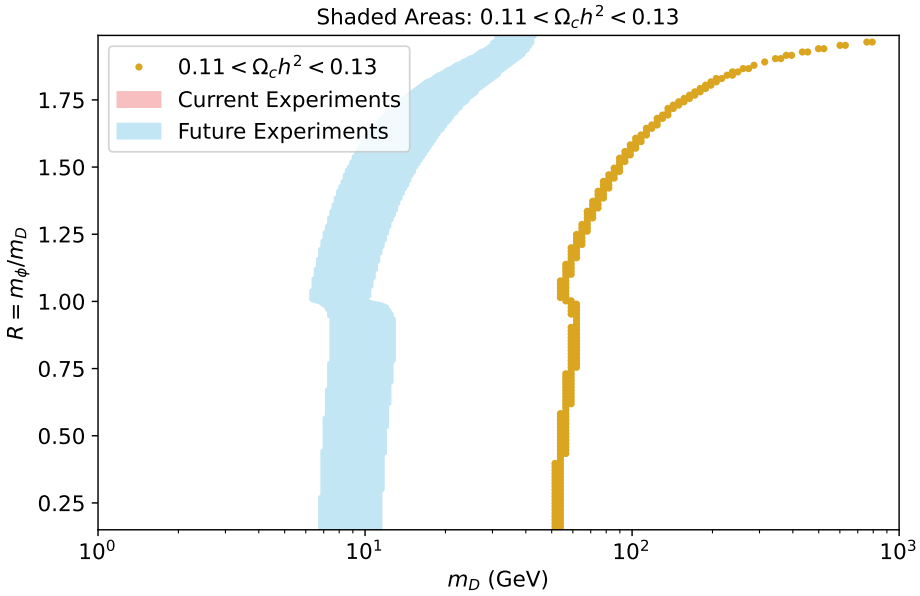

Figure 7.2: Parameter space excluded by the observed neutrino flux for $g_\mathrm{x} = g_\mathrm{n} = 0.1$ compared to combinations of m_D and m_ϕ with a relic density of $0.11 < \Omega_\mathrm{c} h^2 < 0.13$. The latter is obtained from a simulation with `micrOMEGAs`. The basis for the limits shown is the work of [23].

While not even next-generation neutrino detectors will be sufficient to rule out this DM model, it is promising that the gap between the DM masses excluded by neutrino detection and the DM masses leading to the observed relic density shown in Fig. 7.2 is likely to be almost halved by neutrino detection experiments currently under construction/ in planning.

8 Conclusion and Outlook

This thesis investigates the hidden sector specified in Section 2.3 as an extension of the standard model to explain the observed DM relic density of $\Omega_c h^2 = 0.120 \pm 0.001$ [1].
For this purpose, the Boltzmann equation Eq. 4.12 needs to be solved numerically. This differential equation contains the annihilation cross sections of the DM candidate, the leading order of which is calculated using Feynman rules in Chapter 5. These cross sections are then used to solve the Boltzmann equation in `MATLAB`.
The results of the simulations is best summarized in Fig. 6.6: The restriction to the observed relic density only allows for a very limited mass region for set couplings. However, since there are almost no other restriction on the parameters, the couplings are not limited and so a wide range of masses remains viable.
Comparing the results for the relic density of `micrOMEGAs` to those of `MATLAB` shows systematic differences with two main contributions: One are the values used for the degrees of freedom and the other is the fact that the simulation in `MATLAB` uses an s-wave approximation to extrapolate until today's temperature. The total error generally stays within 5 % but increases rapidly around the resonance of $\sigma_{D\bar{D}\to\nu\bar{\nu}}$ to values of up to 15 %. A better approximation would be to include the higher order p-wave annihilations or to approximate the modified Bessel functions for low temperatures instead of the cross sections.
In principle, other restrictions include the decay width of the scalar mediator ϕ which has to be limited to $< 1\,\mathrm{s}$ so that no additional neutrinos are injected during the decoupling of protons and neutrons as predicted by ΛCDM. However, this restriction only excludes extremely light m_ϕ and very small couplings to neutrinos.
More importantly, the DM model produces a flux of neutrinos which can be compared to the observed neutrino flux. As Fig. 7.2 shows, the data of existing experiments excludes masses within an order of magnitude of those necessary to explain the observed relic density and the next generation of neutrino detectors is expected to almost halve this gap. So while neutrino detection is not yet sensitive enough to exclude additional parts of the parameter space, progress is being made.
There is further work to be done in studying this model. This includes the case of heavy ϕ with $m_\phi \geq 2m_\mathrm{D}$ as well as the case when ϕ is not in equilibrium during the decoupling of D and $\bar{D}$. Both require coupled differential equations for ϕ, D and $\bar{D}$. In addition, there is

also the case of non-diagonal couplings $g_{\mathrm{n_{ij}}}$ and $g'_{\mathrm{n_{ij}}}$ to consider. And beyond that, a freeze-in scenario as opposed to the freeze-out studied in this thesis is another possibility.

A Feynman Rules

Feynman rules are a powerful tool to calculate the matrix element $\mathcal{M}$ for all kinds of processes. They allow the elements in the Feynman diagram of the process to be identified with expressions so that the whole Feynman diagram not only functions as a visualisation of the process but also encodes $\mathcal{M}$.
The two dimensions of Feynman diagrams correspond to an axis of time and one of space. In the diagrams shown in this thesis, the earliest events in time are on the left while the latest are on the right. The direction from top to bottom represents different points in space.
The Lagrangian of the hidden sector Eq. 2.2 allows for two kinds of vertices, one which corresponds to an interaction between two DM fermions and the scalar ϕ and another which corresponds to an interaction between to neutrinos and the scalar ϕ. Both interactions are a Yukawa coupling, the Feynman rules for which are derived e.g. in [17, pp.116]. The vertices can be equated to the respective couplings

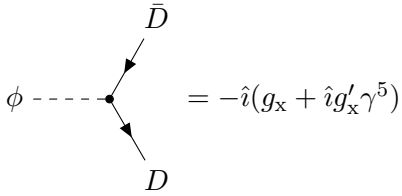

$$= -\hat{\imath}(g_\mathrm{x} + \hat{\imath} g'_\mathrm{x}\gamma^5)$$

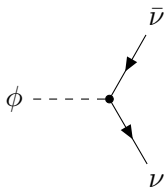

$$= -\hat{\imath}(g_\mathrm{n} + \hat{\imath} g'_\mathrm{n}\gamma^5)\,. \tag{A.1}$$

These equations hold regardless of the orientation of the vertex. In the form above they represent the decay of the scalar but for the purposes of the vertex factor, this is of no consequence.
The above Eq. A.1 makes use of the usual way to represent both scalars and fermions. Dotted lines are scalars. External scalars, which are connected to one vertex, and scalar propagators, which are connected to vertices on both ends and therefore neither an incoming nor an outgoing particle, have different Feynman rules. They are

$$= 1 \qquad \text{and} \qquad$$

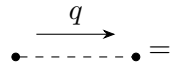

$$= \frac{\hat{\imath}}{q^2 - m_\phi^2 + \hat{\imath}\varepsilon}\,. \tag{A.2}$$

The $\hat{\imath}\varepsilon$ prevents a divergence of the fraction and can be set to 0 at the end of the calculation. Fermions are represented by solid lines with arrows in the middle. If the arrow on the line

points in the direction of negative time, the line represents an anti-fermion. For the four cases of in- and outgoing fermions and anti-fermions, the Feynman rules are

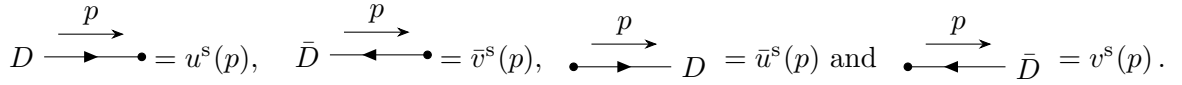

(A.3)

$u^{\mathrm{s}}(p)$ are the general four-spinor solutions to the Dirac equation of a free particle with momentum p and the index $s = 1, 2$ is for the two possible spin states. That is, they fulfill

$$(\hat{\imath}\gamma^{\mu}\partial_{\mu} - m)\psi = 0 \text{ with } \psi = u^{\mathrm{s}}(p)\mathrm{e}^{-ip_{\nu}x^{\nu}} \tag{A.4}$$

$v^{\mathrm{s}}(p)$ are the corresponding negative energy solutions, which are identified with the anti-particle solutions. The barred quantities are defined by $\bar{w} = w^{\dagger}\gamma^{0}$. These fulfill the completeness relations

$$\sum_{s=1,2} \bar{u}^{\mathrm{s}}(p)u^{\mathrm{s}}(p) = \not{p} - m \text{ and } \sum_{s=1,2} \bar{v}^{\mathrm{s}}(p)v^{\mathrm{s}}(p) = \not{p} + m\,, \tag{A.5}$$

where the expression $\not{p} = p_{\mu}\gamma^{\mu}$ is written in Feynman slash notation.
Lastly, fermion propagators can be replaced by

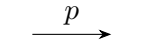

$$= \hat{\imath}\frac{\not{p} + m_{\mathrm{D}}}{p^2 - m^2}\,. \tag{A.6}$$

To construct the diagram of a given process the external lines which represent the incoming and outgoing particles need to be connected using vertices and propagators. These diagrams correspond to terms in time-dependent perturbation theory where the couplings function as a smallness parameter. Therefore, it is usually sufficient to only look at the diagrams with the fewest possible vertices[6].
To get from the diagram to the matrix element the terms along connected fermion lines following the direction of the arrows on the lines need to be multiplied, with the term at the start of the fermion line being the rightmost one and the following terms along the line going to the left of its predecessor. All other terms in the diagrams commute and can be multiplied in whatever order. The momentum of internal lines is defined by four-momentum conservation[7]. This procedure to obtain the matrix element should become more clear by looking at the processes calculated in Chapter 5 as examples.

[6] There can be problems with unitarity, that is probabilities greater than 1, when looking at a limited number of orders [see 6, pp. 463]. In this case, higher order corrections are necessary.
[7] This is not the case for diagrams with 'loops'. These require additional rules. In contrast, the rules in this chapter describe 'tree-level' processes.

B Identities Involving Dirac Matrices

Calculating the matrix elements for processes requires the manipulation of products of Dirac matrices. This chapter lists a collection of useful identities taken from [28, pp. 543], which is a more extensive collection for the general d dimensional Dirac algebra. The identities here are for the usual four-dimensional case.
The defining feature of the Dirac matrices is the anti-commutator

$$\{\gamma^\mu, \gamma^\nu\} = 2\eta^{\mu\nu} \tag{B.1}$$

where $\eta^{\mu\nu}$ is the Minkowski metric with $\eta^{00} = 1$. This property leaves some freedom in choosing the behavior of γ^μ under hermitian conjugation. The usual choice is

$$\gamma^{0\dagger} = \gamma^0,\ \gamma^{\mathrm{k}\dagger} = -\gamma^{\mathrm{k}} \implies \gamma^{\mu\dagger} = \gamma^0\gamma^\mu\gamma^0\,. \tag{B.2}$$

The 'fifth' Dirac matrix γ^5 is defined by

$$\gamma^5 = i\gamma^0\gamma^1\gamma^2\gamma^3\,. \tag{B.3}$$

It does not fulfill the anti-commutator of Eq. B.1 but instead

$$\gamma^{5\dagger} = \gamma^5,\ \gamma^{5\,2} = 1 \text{ and } \left\{\gamma^5, \gamma^\mu\right\} = 0\,. \tag{B.4}$$

Finally, the defining anti-commutator Eq. B.1 leads to a host of useful trace identities for products of Dirac matrices. The relevant ones for this thesis are

$$\text{For any product of an odd number of } \gamma^\mu, \text{ the trace is zero.} \tag{B.5}$$

$$\mathrm{Tr}\left(\gamma^\mu\gamma^\nu\right) = 4\eta^{\mu\nu} \tag{B.6}$$

$$\mathrm{Tr}\left(\gamma^\mu\gamma^\nu\gamma^\rho\gamma^\sigma\right) = 4\left(\eta^{\mu\nu}\eta^{\rho\sigma} - \eta^{\mu\rho}\eta^{\nu\sigma} + \eta^{\mu\sigma}\eta^{\nu\rho}\right) \tag{B.7}$$

$$\mathrm{Tr}\left(\gamma^5\right) = \mathrm{Tr}\left(\gamma^\mu\gamma^\nu\right) = 0 \tag{B.8}$$

$$\text{For } \gamma^5 \text{ times any product of an odd number of } \gamma^\mu, \text{ the trace is still zero.} \tag{B.9}$$

C Simulation Code in MATLAB

This chapter contains the bisection simulation code introduced in Section 6.6. It omits the purely mathematical functions used to implement the Boltzmann equation Eq. 4.12 and the formula for the relic density Eq. 6.2.

```
%this file, called Parameters.m, sets the paramters and constants used during the
%simulation which is done by running SimulatinOfBoltzmannEquationBisect.m.
%Changing the bisection to g_X can be done by looping over values of g_X
%instead of massD and setting bounds on massD analogous to gXToo...
%----------general parameters ----------
%this specifies options for the solver ode15s such as error tolerances
options = odeset('RelTol',1e-5,'AbsTol',1e-100,'Refine',2);
% start and end points of the simulation
%x is m/T in natural units
xStart = 1.0;
xEnd = 350.0;
%simulation interval
criticalInterval = [xStart xEnd];
%---------number of bisection iterations-----
initialIterations = 12;%max iterations to find omega h^2 in densityBounds
rowsSavedData = 26;%number of data rows per massD, massRatio and gN
totalIterations = rowsSavedData-1;%this includes iterations to find edges
%----------bounds on relic density--------
omegaExp = 0.120; % observed value from Planck, 2020
lowerBoundOmegaH2 = 0.11;%lower bound for bisection algorithm
upperBoundOmegaH2 = 0.13;%upper bound for bisection algorithm
densityBounds = [lowerBoundOmegaH2 upperBoundOmegaH2];

%----------constants/parameters in the formulas ----------
gravConstant = 6.7088.*(10.^(-39));%gravitational constant in 1/GeV.^2
constWithSqrtG = sqrt(pi./(45.*gravConstant));
%model parameters to simulate
massD = logspace(0,3,100);%mass of Fermion D
massRatio = linspace(0.1, 1.95, 100);%massRatio between D and Phi
gN = [0.01 0.05 0.1 0.5];%coupling g_nu
%upper and lower bounds on g_X
gXTooLowRelicStart = sqrt(4.*pi);
gXTooHighRelicStart = 1./10.^(4);
%Temperature today in K (from Fixsen, 2009)
tempToday = 2.72528;
tempTodayGeV = 234.891*10.^(-15);
gInternal = 2;% internal degrees of freedom of a fermion
%--------degrees of freedom (Drees, 2018); implemented by A. Abou Ibrahim-----
heff_tab  = load('degrees_of_freedom/heffdhs.dat');%data h_eff
gstar_tab = load('degrees_of_freedom/gstardhs.dat');%data (g*)^(1/2)
geff_tab  = load('degrees_of_freedom/heffdhs.dat');%data g_eff
heff_tmp  = griddedInterpolant(flipud(log(heff_tab(:,1)+1e-100)),...
        flipud(log(heff_tab(:,2))),'pchip');%interpolant for h_eff
gstar_tmp = griddedInterpolant(flipud(log(gstar_tab(:,1)+1e-100)),...
        flipud(log(gstar_tab(:,2))),'linear'); %interpolant for (g*)^(1/2)
geff_tmp  = griddedInterpolant(flipud(log(geff_tab(:,1)+1e-100)),...
        flipud(log(geff_tab(:,2))),'linear'); %interpolant for g_eff
```

```
%solve Boltzmann equation for a given set of parameters
%saving this in a file called Simulate.m allows this to be calles
%with the statement Simulate
[~,Y] = ode15s(@(x,Y) BoltzmannEquation(x,Y, massDCurrent,massPhiCurrent,
    gXCurrent,gNCurrent,constWithSqrtG,gInternal,decayWidthOfPhi,gstar_tab,
    heff_tmp), criticalInterval, initialCondition, options);
YFinal = ProjectToCurrentTemp(xEnd,tempTodayGeV,Y(end,1),massDCurrent,
    massPhiCurrent,gXCurrent,gNCurrent,decayWidthOfPhi,constWithSqrtG,gstar_tmp);
```

```
function resultArray = CalculateMainResults(Y,YToday,massDirac,tempToday,
    densityBounds) % this function calculates the most important results
    resultArray = zeros(1,4);
    resultArray(1,1) = length(Y);%data points in ode15s output
    resultArray(1,2) = YToday;%yield today
    %relic density today
    resultArray(1,3) = DMDensity(resultArray(1,2), massDirac, tempToday);
    if resultArray(1,3) > densityBounds(1,1) ...
        && resultArray(1,3) < densityBounds(1,2)
        resultArray(1,4) = 1;%relic density within bounds
    else
        resultArray(1,4) = 0;%relic density outside bounds
    end
    %one data point: ode15s failed and DM Density will be outside bounds
    resultArray(1,4) = logical(resultArray(1,4)) && logical(resultArray(1,1)-1);
end
```

```
function [newBounds, resultSimul] = CloseInBoundaries(bisectParam,boundTooLow,
    boundTooHigh,Y,YToday,massDirac,tempToday,densityBounds)
%finds the new upper and lower boundaries for the parameter bisectParam
%between which the required relic density can be found.
%only works as long as the relic density is outside densityBounds
    resultSimul = CalculateMainResults(Y,YToday, massDirac,tempToday,
        densityBounds);%main results for current parameters
    if resultSimul(1,1) < 2 || resultSimul(1,3) > densityBounds(1,2)
    %either the relic density was too high or ode15s didn't work.
    %Latter generally happens for very small cross sections -> too high relics
        newBounds(1,2) = bisectParam;
        newBounds(1,1) = boundTooLow;
    elseif logical(resultSimul(1,4))%relic density within bounds
        newBounds(1,2) = boundTooHigh;% Returns original bounds
        newBounds(1,1) = boundTooLow;
    else  %relic density too low
        newBounds(1,2) = boundTooHigh;
        newBounds(1,1) = bisectParam;
    end
end
```

```
function [newBounds, resultSimul] = FindNewBoundaries(bisectParam,boundOutside,
    boundInside,Y,massDirac,tempToday,densityBounds)
%does bisection if  a set of parameters conforming to the relic density bounds
%is found by CloseInBoundaries and closes in on where relic Density = bound
    resultSimul(1,1:4) = CalculateMainResults(Y,YToday,massDirac,tempToday,
        densityBounds); %main results for current parameters
    if logical(resultSimul(1,4))%relic density inside bounds
        newBounds(1,1) = boundOutside;
        newBounds(1,2) = bisectParam;%-> new inside boundary
    else %relic density outside bounds
        newBounds(1,1) = bisectParam;%-> new outside boundary
        newBounds(1,2) = boundInside;
    end
end
```

```
%This script makes use of bisection in the coupling gX to find
%parts of the parameter space which give the correct relic density
%more quickly than simply looping over all model parameters.

%-------intializing parameters--------
Parameters
%-------looping over the desired simulation parameters set in Parameters.m
for k=1:length(gN)
    gNCurrent = gN(1,k);
for j=1:length(massRatio)
    massRatioCurrent = massRatio(1,j);
for l=1:length(massD)
    massDCurrent = massD(1,l);
%-------setting intitial condition & mass & decay width of scalar portal
%needs to be done before every step in of the bisection if massD is
%desired as the bisection parameter instead of gX
    initialCondition = YEquil(x0, massDCurrent,gInternal, heff_tmp);
    massPhiCurrent = massDCurrent.* massRatioCurrent;
    decayWidthOfPhi = DecayWidthPhiNuNu(massPhiCurrent, gNCurrent);
    totalIterations = rowsSavedData-1;%resetting as pot. changed in prev. iter.
    %these arrays are for saving the most important results
    resultSimul = -3.*ones(rowsSavedData,4);
    simulatedParameters = -10.*ones(rowsSavedData,1);
    %parameters closest to but still outside the desired interval of the
    boundsOuter = -1.*ones(rowsSavedData,2);%relic density
    %parameters inside and closest to the edge of the desired interval of the
    boundsInner = -2.*ones(rowsSavedData,2);%relic density
    %dummy containing the current known bounds
    %in the first loop (1,1) is the outer bound with too low relic density
    currentBounds = zeros(1,2);
%-------simulating parameters where relic density is too low-------
    gXCurrent = gXTooLowRelicStart;
    Simulate
    %getting results for lower boundary
    [currentBounds, resultSimul(1,:)] = CloseInBoundaries(gXCurrent,
        gXTooLowYieldStart,gXTooHighYieldStart,Y,YToday,massDCurrent,tempFinal,
        densityBounds);
    %true if relic density within desired interval and simulation worked
    tooLowBoundFits = logical(resultSimul(1,4));
    tooLowBoundSimulated = logical(resultSimul(1,1)-1);%true if simulation worked
    %saving outer bounds and simulated parameter
    boundsOuter(1,:) = currentBounds;
    simulatedParameters(1,1) = gXCurrent;
    if tooLowBoundFits
        boundsInner(1,:) = gXCurrent.*ones(1,2); %saving inner bounds
    end
    clearvars Y %resetting arrays

%-------simulating parameters where relic density is too high-------
    gXCurrent = gXTooHighRelicStart;
    Simulate
    %getting results for upper boundary
    [currentBounds, resultSimul(2,:)] = CloseInBoundaries(gXCurrent,
        currentBounds(1,1),currentBounds(1,2),Y,YToday,massDCurrent,tempFinal,
        densityBounds);
    %true if relic density within desired interval and simulation worked
    tooHighBoundFits = logical(resultSimul(2,4));
    tooHighBoundSimulated = logical(resultSimul(2,1)-1);%true: simulation worked
    boundsOuter(2,:) = currentBounds; %saving outer bounds
    simulatedParameters(2,1) = gXCurrent;% saving simulated parameter
    if tooHighBoundFits
        boundsInner(2,:) = gXCurrent.*ones(1,2);%saving inner bounds
    end
  clearvars Y %resetting arrays
```

```
%------ main bisection part------------------
    outerBoundsDontFit = not(tooLowBoundFits) && not(tooHighBoundFits);
    if (tooLowBoundSimulated|| tooHighBoundSimulated)...
        && (resultSimul(1,3) < densityBounds(1,2)...
        && resultSimul(2,3) > densityBounds(1,1))
    %ode15s was able to simulate at least one end of the interval boundaries and
    %thus it makes sense to continue simulating. This loop finds an initial set
    %of parameters with the desired relic density
    for i = 3:initialIterations
        gXCurrent = geomean(currentBounds);%settting new parameter
        Simulate
        %get new bounds
        [currentBounds,resultSimul(i,:)] = CloseInBoundaries(gXCurrent,
            currentBounds(1,1),currentBounds(1,2), Y,YToday,massDCurrent,
            tempFinal,densityBounds);
        foundFittingParam = logical(resultSimul(i,4));
        boundsOuter(i,:) = currentBounds; %saving outer bounds
        simulatedParameters(i,1) = gXCurrent;%saving simulated parameter
        clearvars Y%resetting array
    if outerBoundsDontFit && foundFittingParam %relic density fits.
        boundsInner(i,:) = gXCurrent.*ones(1,2);%saving as inner bound
        firstFittingGX = gXCurrent;
        break %Exiting this loop
    elseif outerBoundsDontFit && not(foundFittingParam) %no fitting parameter
        continue%found yet. Keep bisecting
    elseif not(foundFittingParam)%no fitting parameter found
    %and one of the initial bounds has a relic density in the desired interval
        boundsInner(i,:) = boundsInner(i-1,:);
    elseif tooLowBoundFits && foundFittingParam%fitting parameter found
    %and the relic density of gXTooLowRelicStart is within
    %the desired interval for the relic density.
    %Bisect on the edge where the relic density reaches the upper limit
        boundsInner(i,:) = [boundsInner(1,1) gXCurrent];
        currentBounds(1,1) = gXCurrent;
    elseif tooHighBoundFits && foundFittingParam%fitting parameter found
    %and the relic density of gXTooHighRelicStart
    %is within the desired interval for the relic density.
    %Bisect on the edge where the relic density reaches the lower limit
        boundsInner(i,:) = [gXCurrent boundsInner(2,2)];
        currentBounds(1,2) = gXCurrent;
    end
    end

    if i >= initialIterations %no relic density within bounds found
        totalIterations = initialIterations; %resetting totalIterations this way
                                             %makes writing into files easier
    else %continues if fitting parameter found before last iteration
        iterationsLeft = totalIterations -i;
        if logical(mod(iterationsLeft,2))%ensures both boundaries are treated
            iterationsLeft = iterationsLeft+1;%equally
            totalIterations = totalIterations +1;
        end
    refiningIter = iterationsLeft./2;%iterations for each boundary.
%-----this part deals with the boundary with DM Densities at-----
%-----the low end of the desired interval-----
    currentBounds = [boundsOuter(i,1) firstFittingGX];
    gXCurrent = geomean(currentBounds);
    for o = 1:refiningIter
        Simulate
        %get results
        [currentBounds, resultSimul(i+o,:)] = FindNewBoundaries(gXCurrent,
            currentBounds(1,1),currentBounds(1,2), Y,YToday,massDCurrent,
            tempFinal,densityBounds);
        %saving data
        simulatedParameters(i+o,1) = gXCurrent;
```

```
122             boundsOuter(i+o,:) = [currentBounds(1,1) boundsOuter(i,2)];
123             boundsInner(i+o,:) = [currentBounds(1,2) boundsInner(i,2)];
124             gXCurrent = geomean(currentBounds);%setting new parameter
125             clearvars Y %reset array
126         end
127 %------this part deals with the boundary with DM Densities at------
128 %------the high endof the desired interval------
129         currentBounds = [boundsOuter(i,2) firstFittingGX];
130         gXCurrent = geomean(currentBounds);
131         for o = 1:refiningIter
132             Simulate
133             %get results
134             [currentBounds,resultSimul(i+o+refiningIter,:)] = FindNewBoundaries(
                    gXCurrent,currentBounds(1,1),currentBounds(1,2), Y,YToday,
                    massDCurrent,tempFinal,densityBounds);
135             %saving data
136             simulatedParameters(i+o+refiningIter,1) = gXCurrent;
137             boundsOuter(i+o+refiningIter,:) = [boundsOuter(i+refiningIter,1)
                    currentBounds(1,1)];
138             boundsInner(i+o+refiningIter,:) = [boundsInner(i+refiningIter,1)
                    currentBounds(1,2)];
139             gXCurrent = geomean(currentBounds);%setting new parameter
140             clearvars Y %reset array
141         end
142         else %gXTooLowYieldStart and gXTooHighYieldStart where chosen in such a
143             totalIterations = 2; %way that the bisection did not make sense
144         end
145         end
146
147  %-------setting arrays for saving data
148         parametersForSaving = [gNCurrent.*ones(rowsSavedData,1) ...
149         massRatioCurrent.*ones(rowsSavedData,1)...
150         massDCurrent.*ones(rowsSavedData,1) simulatedParameters];
151         parametersForSaving(totalIterations+1:end,:) = ...
152             -11.*ones(rowsSavedData-totalIterations,4);
153         savedArray = [parametersForSaving boundsOuter boundsInner resultSimul];
154         %writing data into csv files
155         writematrix(savedArray, 'AllResults.csv','WriteMode','append')
156         %resetting arrays to ensure no data is transferred to the next iteration
157         clearvars savedArray parametersForSaving finalResultArray
158         clearvars boundsOuter boundsInner simulatedParameters resultSimul
159 end
160 end
161 end
```

Bibliography

[1] Planck Collaboration. "Planck 2018 results-VI. Cosmological parameters". In: *Astronomy & Astrophysics* 641 (2020), A6. arXiv: 1807.06209.

[2] Katherine Garrett and Gintaras Duda. "Dark Matter: A Primer". In: *Advances in Astronomy* 2011 (2011), pp. 1–22. arXiv: 1006.2483.

[3] Gianfranco Bertone and Dan Hooper. "History of dark matter". In: *Reviews of Modern Physics* 90.4 (Oct. 2018). arXiv: 1605.04909.

[4] Aaron S. Chou et al. *Snowmass Cosmic Frontier Report*. 2022. arXiv: 2211.09978.

[5] Nicholas L. Rodd. "Listening to the Universe through Indirect Detection". PhD thesis. MIT, 2018. arXiv: 1805.07302.

[6] Mathew D. Schwartz. *Quantum Field Theory and the Standard Model*. Cambridge University Press, 2014.

[7] Jakob Schwichtenberg. *Physics from Symmetry*. 2nd ed. Springer Cham, 2018.

[8] Gertrud Hönes et al. *Neutrinos: Grundlegende Erkenntnisse durch rätselhafte Teilchen*. URL: https://www.mpg.de/neutrinos-grundlegende-erkenntnisse-durch-raetselhafte-teilchen.

[9] Susanne Mertens. "Direct Neutrino Mass Experiments". In: *Journal of Physics: Conference Series* 718 (May 2016), p. 022013. arXiv: 1605.01579.

[10] Werner Tornow. *Search for Neutrinoless Double-Beta Decay*. 2014. arXiv: 1412.0734.

[11] Daniel Baumann. *Cosmology*. The source used are the lecture notes, now turned into a book of the same name.

[12] Martin Bauer and Tilman Plehn. *Yet Another Introduction to Dark Matter*. 2018. arXiv: 1705.01987.

[13] Manuel Drees, Fazlollah Hajkarim, and Ernany Rossi Schmitz. "The effects of QCD equation of state on the relic density of WIMP dark matter". In: *Journal of Cosmology and Astroparticle Physics* 2015.06 (June 2015), p. 025. arXiv: 1503.03513.

[14] Edward Kolb and Michael Turner. *The early universe*. Avalon Publishing, 1994.

[15] Paolo Gondolo and Graciela Gelmini. "Cosmic abundances of stable particles: Improved analysis". In: *Nuclear Physics B* 360.1 (1991), pp. 145–179. DOI: https://doi.org/10.1016/0550-3213(91)90438-4.

[16] Eric W. Weisstein. *Modified Bessel Function of the Second Kind*. From Mathworld–A Wolfram Web Resource. URL: https://mathworld.wolfram.com/ModifiedBesselFunctionoftheSecondKind.html.

[17] Michael E. Peskin and Daniel V. Schroeder. *An Introduction to Quantum Field Theory*. Addison-Wesley, 1995.

[18] University of Southampton. *Lorentz Invariant Phase-Space*. URL: https://southampton.ac.uk/~doug/ft1/ft19.pdf.

[19] The MathWorks, Inc. *MATLAB® Release Notes*. 2023. URL: https://www.mathworks.com/help/pdf_doc/matlab/rn.pdf.

[20] Geneviève Bélanger et al. *MicrOMEGAs: a code for the calculation of Dark Matter Properties*. 2022. URL: https://lapth.cnrs.fr/micromegas/.

[21] The MathWorks, Inc. *Ordinary Differential Equations*. URL: https://de.mathworks.com/help/matlab/ordinary-differential-equations.html.

[22] D. J. Fixsen. "The Temperature of the Cosmic Microwave Background". In: *The Astrophysical Journal* 707.2 (Nov. 2009), pp. 916–920. arXiv: 0911.1955.

[23] Carlos A. Argüelles et al. "Dark matter annihilation to neutrinos". In: *Reviews of Modern Physics* 93.3 (Sept. 2021). arXiv: 1912.09486.

[24] G. Bélanger et al. "micrOMEGAs_3: A program for calculating dark matter observables". In: *Computer Physics Communications* 185.3 (Mar. 2014), pp. 960–985. arXiv: 1305.0237.

[25] Keith A. Olive, David N. Schramm, and Gary Steigman. "Limits on new superweakly interacting particles from primordial nucleosynthesis". In: *Nuclear Physics B* 180.3 (1981), pp. 497–515. DOI: https://doi.org/10.1016/0550-3213(81)90065-1.

[26] Mark Srednicki, Richard Watkins, and Keith A. Olive. "Calculations of relic densities in the early universe". In: *Nuclear Physics B* 310.3 (1988), pp. 693–713. DOI: https://doi.org/10.1016/0550-3213(88)90099-5.

[27] Ankit Rohatgi. *WebPlotDigitizer: Version 4.6*. 2022. URL: https://automeris.io/WebPlotDigitizer.

[28] Walter Greiner, Stefan Schramm, and Eckart Stein. *Quantum Chromdynamics*. 3rd ed. Springer Berlin, Heidelberg, 2007.